Ulm University Medical Center
Department of Internal Medicine II
Head: Prof. Dr. W. Rottbauer

Respiratory and Cardiac Self-Gated Radial MRI

Dissertation to Obtain the Doctoral Degree
of Human Biology (Dr. biol. hum.)
of the Medical Faculty of Ulm University

Submitted by Jan Paul, born in Karlsruhe

2015

Acting Dean: Prof. Dr. T. Wirth
First Reviewer: Prof. Dr. V. Rasche
Second Reviewer: Prof. Dr. A. Nagel
Date of Graduation: January 22, 2016

Contents

Abbreviations **iv**

1 Motivation **1**

2 Theory **3**
2.1 MR Signal Generation and Image Contrast 3
2.2 Spatial Encoding 4
2.3 Image Reconstruction 5
2.4 Golden Angle Radial MRI 9
2.5 Respiratory Motion 11
2.6 Tissue Phase Mapping (TPM) 12
2.7 Cardiac Motion 15

3 Methods **17**

4 Comparison of Different Self-Gating Methods (Reprinted Article) **20**

5 Combination of Respiratory Self-Gating and Tissue Phase Mapping (Reprinted Article) **28**

6 Cardiac Self-Gating and Non-Uniform Self-Gating (Reprinted Article) **41**

7 Results and Discussion **49**

Bibliography **52**

List of Figures **54**

List of Tables **55**

Acknowledgments **56**

Curriculum Vitae **57**

Abbreviations

ACQ	Acquisition.
bSSFP	Balanced Steady-State Free Precession.
CAD	Coronary Artery Disease.
COM	Center of Mass.
CRT	Cardiac Resynchronization Therapy.
CS	Compressed Sensing.
ECG	Electrocardiogram.
FLASH	Fast Low Angle Shot.
FOV	Field of View.
GA	Golden Angle.
GRAPPA	Generalized Autocalibrating Partial Parallel Acquisitions.
HF	Heart Failure.
IDFT	Inverse Discrete Fourier Transform.
IFFT	Inverse Fast Fourier Transform.
LV	Left Ventricle.
MRI	Magnetic Resonance Imaging.
nuSG	Non-Uniform Self-Gating.
PC	Phase Contrast.
PCA	Principal Component Analysis.
PSF	Point Spread Function.

RF Radio Frequency.
RMSE Root Mean Square Error.
RNAV Respiratory Navigator.
ROI Region of Interest.

SENSE Sensitivity Encoding.
SG Self-Gating.
SNR Signal to Noise Ratio.

TMJ Temporomandibular Joint.
TPM Tissue Phase Mapping.
TV Total Variation.

VENC Velocity Encoding.

1 Motivation

Motion in cardiac *Magnetic Resonance Imaging (MRI)* is a major challenge, as it results in artifacts like image blurring if not compensated for.

Respiratory motion of the heart can be addressed by acquisitions during breath-hold for scan times shorter than 10–15 seconds. When longer scans are required, only data from end-expiration is used. Determination of the respiratory position is typically achieved via interleaved *Respiratory Navigator (RNAV)* measurements (see section 2.5). *Self-Gating (SG)* is an alternative method for generating a respiration signal, overcoming some of the challenges associated with the traditional method.

Measurement of motion velocities during the heartbeat via *Tissue Phase Mapping (TPM)-MRI* intrinsically requires long acquisition times and thus necessitates consideration of respiratory motion. *TPM* allows quantification of global and regional myocardial motion and is clinically relevant to understand cardiac motion abnormalities, e.g. in cases of *Heart Failure (HF)* [4] or *Coronary Artery Disease (CAD)* [2]. This might also support treatment decisions, as for implantation of a biventricular pacemaker in *Cardiac Resynchronization Therapy (CRT)*, where ca. 30% of the treated patients currently show no improvement from this therapy [20, 19]. Among different *MRI* acquisition methods for analysis of myocardial mechanics [16], *TPM* can provide precise and reproducible three-dimensional velocity information of the heart muscle over the complete cardiac cycle [15], which can also be used for derivation of strain-based motion parameters [7, 9] as known from ultrasound or other *MRI* imaging sequences.

Cardiac motion, i.e. the heartbeat itself, also has to be considered to achieve motion-free images or time-resolved cine movies of the beating heart. *SG* can also be applied for cardiac synchronization as an alternative to the traditional method of *Electrocardio-*

gram (ECG)-based gating (see section 2.7). Furthermore, cardiac *SG* can be extended to be able to resolve non-uniform cardiac motion, e.g. in case of arrhythmia.

The aim of this thesis is to investigate *SG* as an alternative to current respiratory and cardiac gating methods. Respiratory *SG* is applied for *TPM* in combination with *Compressed Sensing (CS)* reconstruction of undersampled data for reduction of acquisition time, and cardiac *SG* is investigated for resolving cardiac motion and cardiac arrhythmia.

Basic *MRI* concepts and special methodology used in this thesis are described in chapter 2. The main methods are outlined in chapter 3. Different *SG*-variants are compared in chapter 4. The most promising method is applied to resolve respiratory motion with *TPM*, where higher temporal resolution is required (see chapter 5). In chapter 6, *SG* is investigated for even higher temporal resolution by application for cardiac gating and non-uniform synchronization, based on the findings of chapter 4. Finally, the results are summarized and discussed in chapter 7.

2 Theory

2.1 MR Signal Generation and Image Contrast

Magnetic Resonance Imaging (MRI) is based on quantum-mechanical properties of protons (^{1}H), which are abundant in the human body mainly in form of water and fat. A proton's spin is considered in the classical interpretation as the rotation around its own axis, which creates a microscopic magnetic field.

When exposed to an external magnetic field $\mathbf{B}_0$ (oriented along the z-axis), the protons' spins are aligned either parallel (spin up) or anti-parallel (spin down) to the magnetic field, where the ratio is slightly towards more parallel orientations (the lower energy state), resulting in a net magnetization vector $\mathbf{M}$ in the direction of $\mathbf{B}_0$. Rotation of $\mathbf{M}$ around $\mathbf{B}_0$ with the Larmor frequency $\omega_0 = \gamma B_0$ and the gyromagnetic ratio of $\gamma = 42.6\,\mathrm{MHz/T}$ can be described by the Bloch equation $\frac{\mathrm{dM(t)}}{\mathrm{d}t} = \gamma \mathbf{M}(t) \times \mathbf{B}_0$.

Application of a *Radio Frequency (RF)* pulse flips $\mathbf{M}$ towards the xy-plane, resulting in a decrease of longitudinal magnetization M_z and increase of transversal magnetization M_{xy}, where the latter can be measured via electromagnetic induction (due to the magnetization's rotation around the z-axis) by receiver coils.

After excitation, the net magnetization vector $\mathbf{M}$ turns back towards the z-axis, as this is the energetically optimal state (thermal equilibrium). The effect is due to spin-lattice interaction, where the spins' energy is dissipated to the surrounding molecules. This relaxation of longitudinal magnetization over time t can be described by $M_z(t) = M_0 \cdot (1 - e^{-t/T_1})$, where the tissue-dependent constant T_1 describes the time of recovery of 63% of the original longitudinal magnetization M_0.

Also, the magnetization vectors of different protons start to dephase due to local fluctuations (spin-spin interaction) and inhomogeneities of the magnetic field, reducing the net transversal magnetization over time t as $M_{xy}(t) = M_0 \cdot e^{-t/T_2^*}$. The tissue-dependent constant T_2^* describes the time when the 37%-level of the original magnetization M_0 is reached. Dephasing effects resulting from magnetic field inhomogeneities can be undone by rephasing via "spin echo", thus prolonging the decay to $M_{xy}(t) = M_0 \cdot e^{-t/T_2}$, with $\frac{1}{T_2^*} = \frac{1}{T_2} + \frac{1}{T_2'}$ where T_2' is the decay constant for the field inhomogeneity effects.

Image contrast between tissues can be obtained by exploiting the different proton densities and relaxation constants (e.g. approximately T_1: 250 ms for fat, 1300 ms for blood, 900 ms for muscle; and T_2: 70 ms for fat, 300 ms for blood, 50 ms for muscle; with $B_0 = 1.5\,\mathrm{T}$), which in turn yield different transversal magnetizations M_{xy} at measurement time t.

2.2 Spatial Encoding

Spatial encoding is achieved by application of gradients $\mathbf{G}(t) = (G_x(t), G_y(t), G_z(t))^\top$ (linear magnetic fields), which allow to uniquely distinguish the signals from each location by locally changing the Larmor frequency. The signal s measured at time t is related to the transversal magnetization M_{xy} of the measured object at location $\mathbf{r}$ by the Fourier transform $\mathcal{F}$, since [3]:

$$s(t) = s(\mathbf{k}) = \int_0^t M_{xy}(\mathbf{r}) \cdot e^{-i2\pi \cdot \mathrm{k}(t) \cdot \mathrm{r}} \mathrm{d}\mathbf{r} = \mathcal{F}[M_{xy}(\mathbf{r})]. \tag{2.1}$$

The traversal of measurement positions (trajectory) in frequency space (k-space) is described as

$$\mathbf{k}(t) = \gamma \int_0^t \mathbf{G}(t')\mathrm{d}t' \tag{2.2}$$

and can be controlled via the gradients. Selection of a specific coordinate $\mathbf{k}$ is achieved by phase encoding gradients, and the readout of several signal points along a line (profile) in k-space is performed via frequency encoding gradients. K-space is filled by multiple repetitions of such readouts in different k-space positions.

In conventional Cartesian *MRI*, every line of samples is acquired in a parallel fashion, whereas in radial *MRI* every profile traverses the k-space center (see Figure 1c-d). Cartesian imaging is achieved by increasing the phase encoding gradient linearly in every repetition, while the frequency encoding gradient remains the same. For radial acquisitions, both in-plane gradients are scaled in every repetition with a sin / cos-pattern, yielding rotation around the k-space center (Figure 1a-b).

Due to gradient imperfections such as eddy currents, the trajectory $\mathbf{k}(t)$ is not traversed precisely as defined. In Cartesian acquisitions, the trajectory error is a constant shift in k-space along the same direction, yielding the same linear phase in image space. As this does not affect image quality, no corrections need to be performed when reconstructing Cartesian image data. For radial encoding however, the trajectory errors vary with the profile direction, resulting in destructive interference and thus degraded image quality. Therefore, these errors are estimated using almost opposite profiles and a correction is performed before image reconstruction [14].

2.3 Image Reconstruction

Image reconstruction can be described in a matrix-vector notation, where both the image $\mathbf{x}$ (as a discrete version of $M_{xy}(\mathbf{r})$) and the acquired k-space data $\mathbf{b}$ (as a discrete version of $s(\mathbf{k})$) are reformatted into a vector. Signal measurement is described by the forward model $\mathbf{Ax} = \mathbf{b}$, and image reconstruction is denoted in the backward model as $\mathbf{x} = \mathbf{A}^{-1}\mathbf{b}$, where $\mathbf{A}$ is the system encoding matrix and $\mathbf{A}^{-1}$ its inverse.

In the simplest case of Cartesian imaging with a single receiver coil, the measured signal is the discrete Fourier transform of the image (Eq. 2.1), i.e. $\mathbf{A} = \mathbf{F}$, and can be efficiently reconstructed via *Inverse Discrete Fourier Transform (IDFT)* $\mathbf{A}^{-1} = \mathbf{F}^{H}$

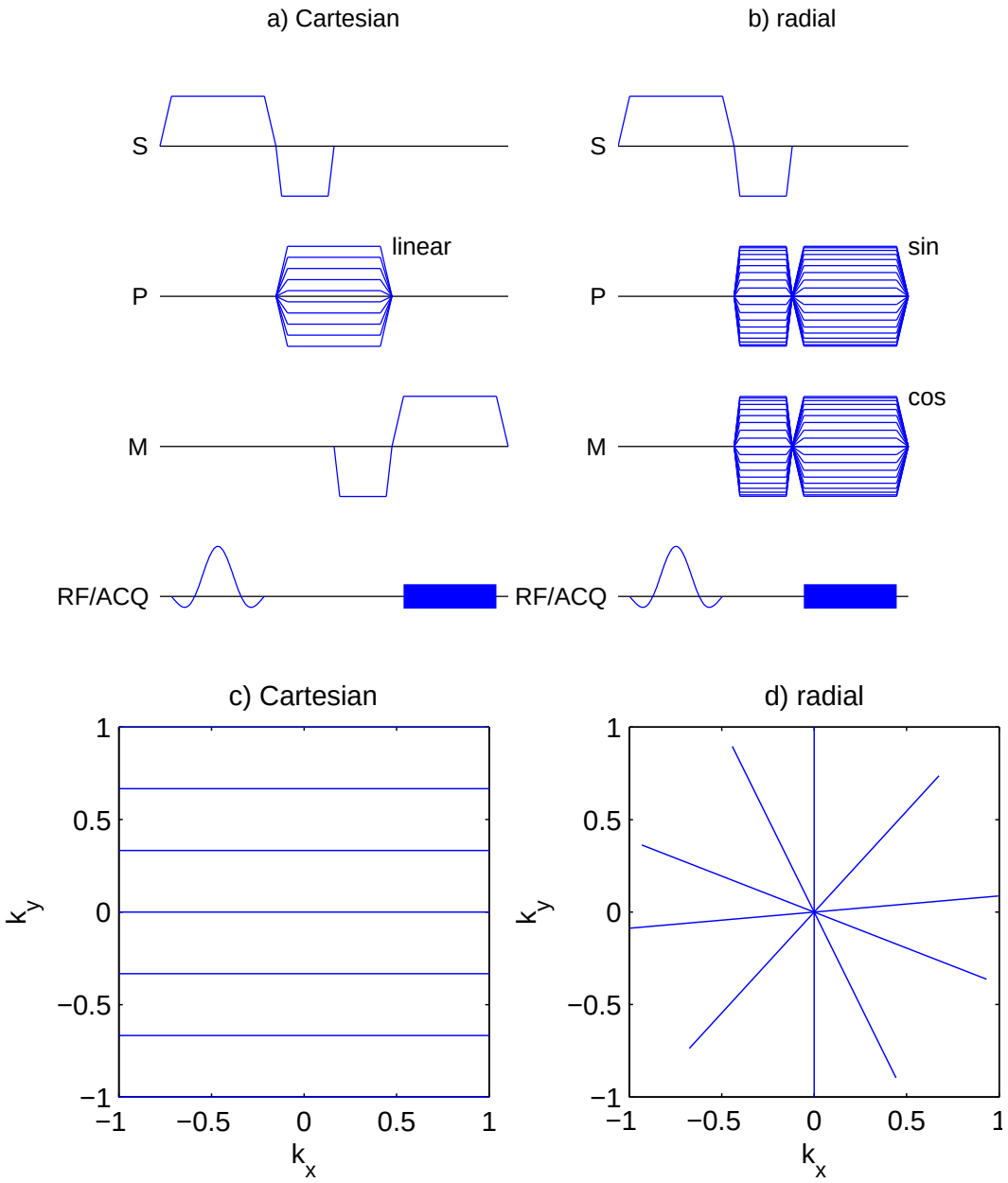

Figure 1: Comparison of Cartesian (a) and radial (b) *Magnetic Resonance Imaging (MRI)* sequence diagrams and respective Cartesian (c) and radial (d) k-space trajectories. For display purposes, only few of the acquired lines are shown. Abbreviations: *Radio Frequency (RF)*, *Acquisition (ACQ)*

with the *Inverse Fast Fourier Transform (IFFT)* algorithm. Using more than one coil element requires consideration of different coil sensitivity profiles $\mathbf{S}$, so that $\mathbf{A}^{-1} = \mathbf{S}^H\mathbf{F}^H$. For radial trajectories, the k-space data is measured at non-integer positions. Hence, $\mathbf{F}^H$ is the non-uniform (i.e. weighted) *IDFT* in this case. As this direct operation is computationally challenging, data are first interpolated onto Cartesian coordinates via gridding convolution, which then allows application of the *IFFT* [8].

For a unique solution of the linear equation system, the same number of sampled k-space points is required as the number of desired image pixels. Often less data is measured for reduction of acquisition time by leaving out k-space profiles, and thus the equation system becomes under-determined. In terms of signal processing, the Nyquist theorem is violated, because the number of profiles N_p is less than the dimension of the image data N_s. For radial imaging, the Nyquist criteria requires even more profiles ($N_p \geq \frac{\pi}{2} N_s$) to ensure that every sample point is measured also at the very outer k-space, although this results in an oversampled central part of k-space. The undersampling factor R is defined as the number of profiles required by the respective Nyquist theorem divided by the number of measured profiles.

Reconstruction of undersampled k-space data by defining the samples not measured to be zero leads to distinct ghosting artifacts in Cartesian imaging, while streaking artifacts result for radial acquisitions (see Figure 2), due to the different *Point Spread Function (PSF)*.

Undersampling artifacts can be reduced to a certain degree by adding additional equations to the system, which in *MRI* is achieved with parallel imaging using multiple receiver coils, thus allowing reconstruction of the missing sample points in image space (e.g *Sensitivity Encoding (SENSE)* [13]) or k-space (e.g. *Generalized Autocalibrating Partial Parallel Acquisitions (GRAPPA)* [5]).

When even more acquisition acceleration is desired, the equation system is still under-determined although including data from several coil elements, and undersampling artifacts result in the reconstructed images. For reduction of these artifacts, the reconstruction is constrained to select one (of the infinitely many) solutions. In *Compressed*

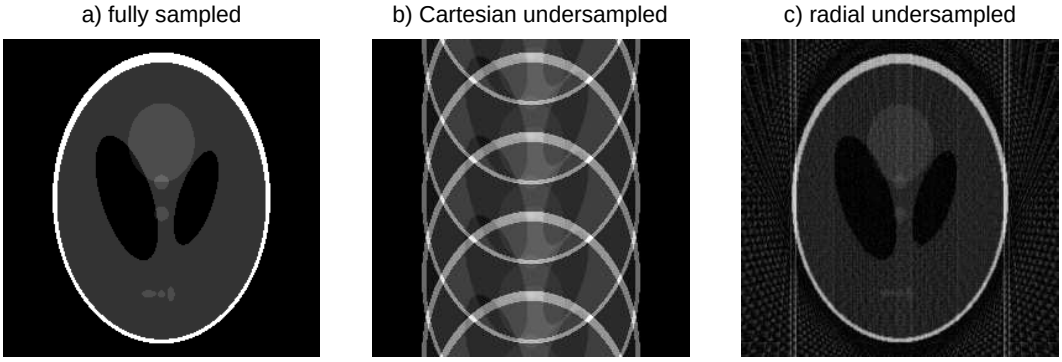

Figure 2: Comparison of artifacts for an undersampling factor of $R = 4$ relative to the respective Nyquist criteria in the Shepp-Logan phantom (a): for a Cartesian (b) and a radial (c) trajectory.

Sensing (CS) MRI [6], the reconstruction then becomes a regularized approach solved as a non-linear minimization problem of the form

$$\mathbf{x}^* = \underset{x}{\operatorname{argmin}} \|\mathbf{A}\mathbf{x} - \mathbf{b}\|_2^2 + \lambda \|\nabla_t \mathbf{x}\|_1 \tag{2.3}$$

The ℓ_2-norm enforces similarity of the k-space $\mathbf{A}\mathbf{x}$ (corresponding to the reconstructed image $\mathbf{x}$) to the measured k-space $\mathbf{b}$, and the *Total Variation (TV)* (ℓ_1-term) penalizes artifacts by summation of the temporal derivative ∇_t of the image. The amount of regularization is determined by the application-specific scalar λ.

CS theory requires three preconditions, which can be fulfilled for *MRI* [6]:

- transform into a sparse domain: since *MRI* images of human anatomy are approximately spatially piecewise constant and move continuously, the temporal derivative is close to zero everywhere except at tissue boundaries during motion;
- noise-like (incoherent) undersampling artifacts: streaking in radial sampling;
- non-linear reconstruction: is achieved by solving the described minimization problem (Eq. 2.3).

While Cartesian sampling (also in combination with parallel imaging) allows simple non-iterative reconstruction using mainly inverse Fourier transformation, radial reconstruction is computationally more demanding due to additional gridding step, especially in combination with *CS*, where several gridding and re-gridding operations are required to perform iterative functional minimization.

2.4 Golden Angle Radial MRI

Golden Angle (GA) MRI [17] is a special form of radial trajectory where the angular increment between subsequent radial profiles is $\Delta\theta = \frac{180^\circ}{\tau} \approx 111.25^\circ$, based on the golden ratio $\tau = \frac{1+\sqrt{5}}{2} \approx 1.618$. It has been proven [17] that any number of consecutive radial profiles acquired with the *GA* scheme cover the k-space highly uniformly.

Thus, a sliding window reconstruction of partially overlapping windows of radial profiles allows a time-resolved reconstruction of the acquired data (see Figure 3a). The width of the sliding window (i.e. the number of profiles) defines the temporal resolution in terms of temporal blurring but also the level of undersampling artifacts. The shift between sliding windows (i.e. the amount of overlap) allows selection of the reconstructed frame-rate. Additionally, as in any radial acquisition scheme, the reconstructed spatial resolution can be reduced independently of the temporal resolution by removing high-frequency parts of the radial k-space profiles (see Figure 3a-c), thus reducing undersampling artifacts for a given temporal resolution. In combination with *CS*, the artifact level can be further reduced.

In summary, radial (especially *GA*) trajectories compare to Cartesian acquisition as described in Table 2.

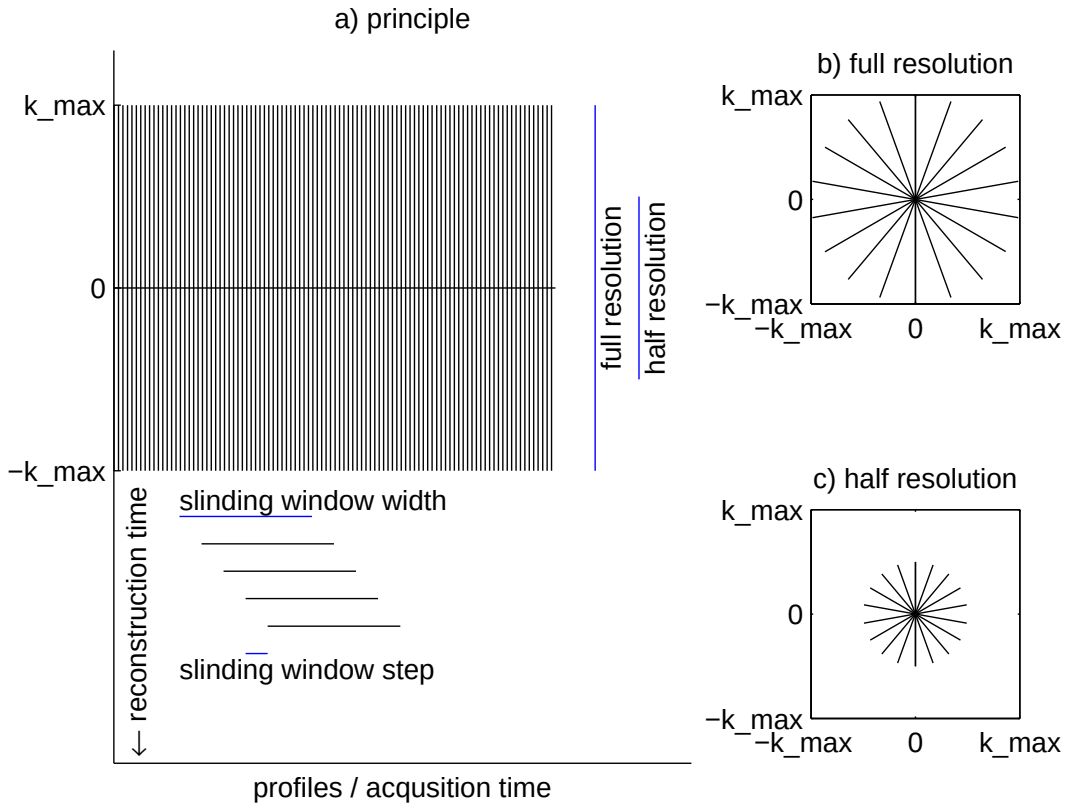

Figure 3: Principle of sliding window reconstruction. Frames are reconstructed from overlapping parts of radial profiles, determining the temporal resolution (a). Spatial resolution is determined by the range of k-space frequencies used for reconstruction (b, c).

Table 2: Comparison of Cartesian and radial *Magnetic Resonance Imaging (MRI)*. N_p = number of profiles, N_s = number of reconstructed points (in one dimension). Abbreviations: *Compressed Sensing (CS)*, *Golden Angle (GA)*.

Property	Cartesian	Radial
Nyquist criteria	$N_p \geq N_s$	$N_p \geq \frac{\pi}{2} N_s \approx 157\% \cdot N_s$
Undersampling artifacts	ghosting	streaking
Trajectory corrections	none	radial offsets
Reconstruction	fast	slower (gridding required)
Sliding window reconstruction	possible with view sharing	possible for *GA*
CS reconstruction	needs random phase encoding	possible with *GA*

2.5 Respiratory Motion

To avoid motion artifacts like blurring, respiration has to be considered in *MRI* acquisitions of the heart. When the scan time is longer than 10–15 seconds and thus the acquisition cannot be performed during breathhold, other means of respiratory motion compensation have to be applied.

The conventional approach is to interleave the imaging with a navigator sequence, where the position of the liver is measured repeatedly by a *Respiratory Navigator (RNAV)*, see Figure 4. Imaging data acquired during end-expiration are used for reconstruction, whereas data measured during inhalation, exhalation or end-inspiration are rejected. This leads to a navigator efficiency (data acceptance rate) of 50%–60%, which further prolongs scan time.

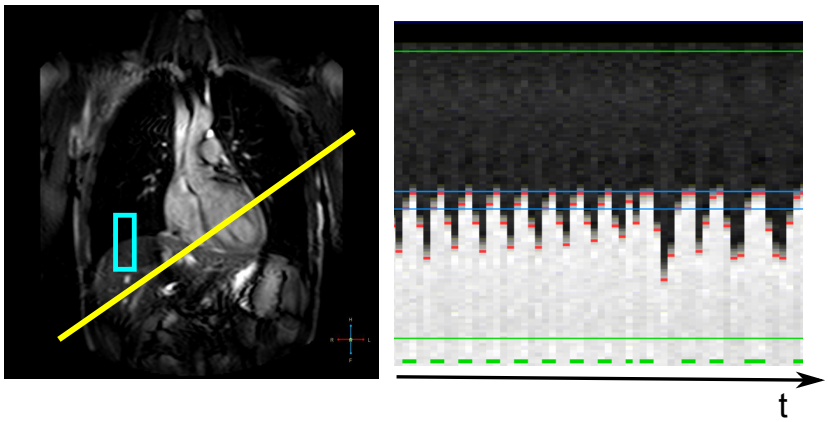

Figure 4: Coronal view (left) with position of the *Respiratory Navigator (RNAV)* (blue) on the liver and imaging slice (yellow); navigator signal over time (right) with acceptance window (blue) and acceptance markers (green, bottom).

Several disadvantages arise from *RNAV* measurements. The steady state of the imaging sequence has to be interrupted, the separate navigator measurement takes additional time, and it might interfere with the imaging blood suppression volume.

An alternative to *RNAV* is respiratory *Self-Gating (SG)*, where the respiration state is derived from the imaging data itself, thus eliminating the necessity for a separate interleaved measurement, as investigated in chapter 4.

2.6 Tissue Phase Mapping (TPM)

Phase Contrast (PC)-MRI allows to measure the velocity of an imaged object. First, the one-dimensional case is considered [3, 1].

Application of a gradient G at location r along the one axis results in a phase shift of

$$\varphi(t) = \gamma \int_0^t G(t')r(t')\,\mathrm{d}t' \tag{2.4}$$

where $t' = 0$ is at the beginning of the gradient application.

Considering motion $r(t') = r_0 + v \cdot t'$ along the axis of gradient application, with constant velocity v (neglecting acceleration and higher order terms), yields

$$\begin{aligned}\varphi(t) &= \gamma \int_0^t G(t') \cdot (r_0 + v \cdot t')\ \mathrm{d}t' \\ &= \gamma r_0 \int_0^t G(t')\,\mathrm{d}t' + \gamma v \int_0^t G(t')t'\,\mathrm{d}t' \\ &= \gamma \cdot (r_0 m_0 + v m_1)\end{aligned} \tag{2.5}$$

with the zeroth and first gradient moments, m_0 and m_1, respectively.

While m_0 (the gradient area) is translation invariant, m_1 depends on the time shift T after the start of the gradient by $m_1(T) = m_0 T + m_1(0)$ [1].

Consider application of a bipolar gradient, i.e. two gradient lobes with same area but opposite sign in direct succession, each lobe with a duration T. The gradient moments of the first lobe are

$$m_0^+ := m_0 \qquad \text{and} \qquad m_1^+ := m_1, \tag{2.6}$$

and the moments of the second lobe are

$$m_0^- = -m_0 \qquad \text{and} \qquad m_1^- = m_1^-(T) = m_0^- \cdot T + m_1^-(0) = -m_0 \cdot T - m_1. \tag{2.7}$$

since it is applied directly after the first lobe, i.e. starting at $t = T$ and ending at $t = 2T$.

Thus, the phase after application of a bipolar gradient yields

$$\begin{aligned}\varphi(2T) &= \varphi_+ + \varphi_- \\ &= \gamma \cdot \left(r_0 \cdot m_0^+ + v \cdot m_1^+\right) + \gamma \cdot \left(r_0 \cdot m_0^- + v \cdot m_1^-\right) \\ &= \gamma \cdot (r_0 \cdot m_0 + v \cdot m_1 - r_0 \cdot m_0 - v \cdot (m_0 \cdot T + m_1)) \\ &= -\gamma \cdot v \cdot m_0 \cdot T.\end{aligned} \tag{2.8}$$

From Eq. 2.8, the velocity can be calculated as $v = \frac{-\varphi}{\gamma \cdot m_0 \cdot T}$. Since the phase is in the range of $[-\pi..\pi]$, the highest measurable velocity, or *Velocity Encoding (VENC)*, is $v_{\text{enc}} = \frac{\pi}{\gamma \cdot m_0 \cdot T}$. When velocities higher than v_{enc} occur, they will be aliased back to the range $[-v_{\text{enc}}..v_{\text{enc}}]$ due to phase wrapping of φ.

However, only the velocity in the direction of the bipolar gradient is measured. To obtain the velocity in all three directions, bipolar gradients are subsequently applied on all three gradient axes, each repetition measuring velocities along one axis. A fourth measurement is added for reference, to be able to remove phase effects not related to velocity. In the 4-point balanced scheme (Hadamard encoding) the bipolar gradients are not applied on one axis at a time, but on all axes in every repetition (see Figure 5) with different signs of the gradient lobes (see Table 3) [12]. Thus, every velocity along the image coordinate system is obtained from all four rather than two measurements, leading to *Signal to Noise Ratio (SNR)* improvement. The velocities are calculated via summation of the phases obtained from separated reconstructions of the four velocity encoding directions (Table 3).

Tissue Phase Mapping (TPM) is the application of *PC-MRI* measurements in three directions to measure time-resolved velocities of the myocardium over the cardiac cycle. For this application, v_{enc} is usually set to 30 cm/s. Acquisition times for *TPM* are more than four-fold compared to non-velocity encoded measurements due to the necessity to acquire four velocity measurement directions and the integration of bipolar gradients into the sequence.

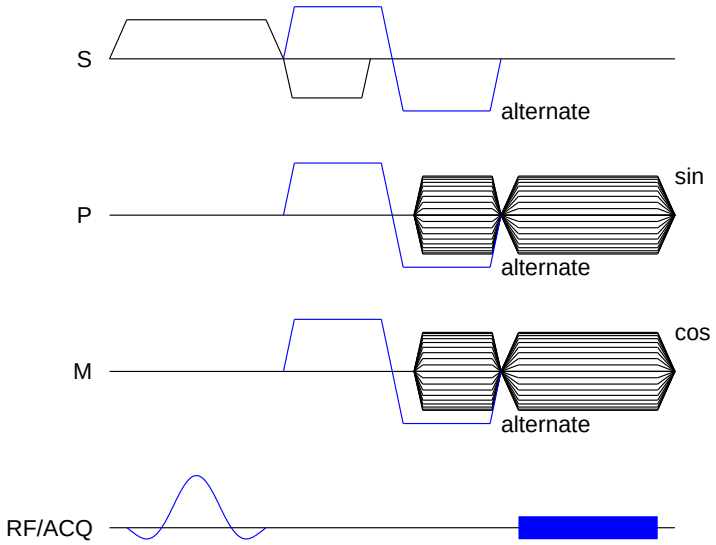

Figure 5: Sequence diagram for radial *Phase Contrast (PC)*-*Magnetic Resonance Imaging (MRI)*. The signs of the bipolar gradients are alternated for different velocity encoding directions according to Table 3. Abbreviations: *Radio Frequency (RF)*, *Acquisition (ACQ)*.

Table 3: Four-point balanced Hadamard encoding scheme for 3D *Phase Contrast (PC)*-*Magnetic Resonance Imaging (MRI)*. Denoted is the sign of the first lobe of each bipolar gradient for the different encoding directions (measurements) and gradient axes. E.g., the phase for calculation of the velocity along M is calculated as $\varphi_M = -\varphi_1 + \varphi_2 + \varphi_3 - \varphi_4$. Source: [12].

Measurement	M	P	S
1	−	−	−
2	+	+	−
3	+	−	+
4	−	+	+

Velocities are transformed into the anatomical coordinate system of radial (contraction–expansion), circumferential (rotation, tangential), and longitudinal (apical–basal) velocities (see Figure 6) after reconstruction.

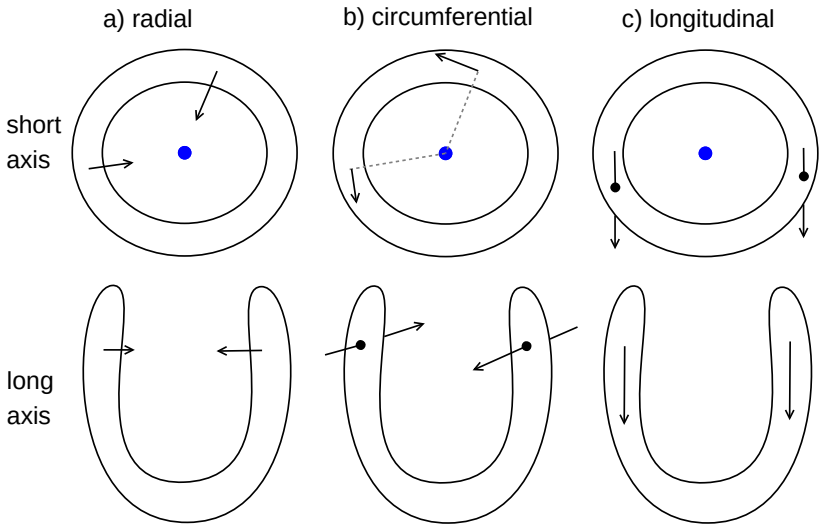

Figure 6: Radial (a), circumferential (b), and longitudinal (c) velocity directions on the myocardium in short axis (top) and long axis (bottom) view of the *Left Ventricle (LV)*. Figure modified from [9].

2.7 Cardiac Motion

During a heartbeat, the ventricles contract to pump blood into the body (systole) and relax to be filled with blood again (diastole). This cardiac motion has to be considered in *MRI* acquisitions of the heart to avoid motion blurring, or to reconstruct time-resolved "cine" data of the beating heart for diagnostic purposes.

Thus, the acquired data needs to be synchronized with, or sorted according to, the phases of the cardiac cycle. This is usually achieved by detecting peaks in an *Electro-*

cardiogram (ECG) (see Figure 7) or in a peripheral pulse oximeter. These peaks define the beginning of a heartbeat and are used to order the data linearly in between.

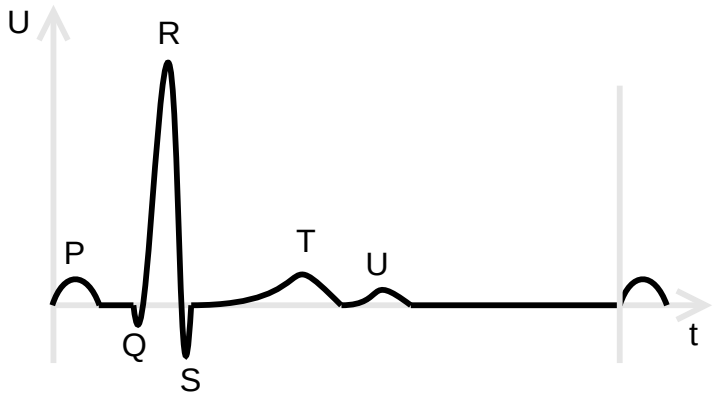

Figure 7: Schematic *Electrocardiogram (ECG)*. The signal for one heartbeat is shown. Peaks are labelled with their defined symbols. The "R" peak is used for cardiac synchronization in *Magnetic Resonance Imaging (MRI)*. Figure from [9].

Disadvantages of the *ECG* are the necessity to place electrodes at the patients chest and the degeneration of signal quality during *MRI* acquisitions due to influence of switching magnetic fields. The pulse oximeter is easier to place and not influenced by the acquisition; however, the detected signal is delayed with respect to the actual heartbeat and results in missing the acquisition of the clinically relevant systole.

Deriving a surrogate signal for cardiac motion from the imaging data itself, i.e. cardiac *SG*, can solve these disadvantages. Furthermore, advanced methods to generate and analyze a cardiac *SG* signal allow imaging of non-uniform cardiac motion, e.g. in patients with arrhythmia, as is investigated in chapter 6.

3 Methods

In this thesis, *Self-Gating (SG)-Magnetic Resonance Imaging (MRI)* was investigated as follows: first, different *SG*-variants were compared (chapter 4) in combination with *Compressed Sensing (CS)* for detection of respiratory motion, then respiratory *SG* was combined with *Tissue Phase Mapping (TPM)* for analysis of myocardial motion (chapter 5), and finally cardiac *SG* was investigated and extended to resolve non-uniform motion (chapter 6).

SG is the generation of a motion surrogate signal (i.e. giving information about a motion state) from the imaging data itself, rather than acquiring separate data to obtain motion information.

For the analysis of respiratory *SG* (chapter 4), different variants of signal generation algorithms were compared, based on the k-space data of the imaging slice. 0D-*SG* describes the use of the k-space center of each radial profile, whereas in 1D-*SG* the sum or *Center of Mass (COM)* was obtained from 1D-Fourier transfomed profiles. All these variants resulted in a complex-valued signal over time, and magnitude, phase, real, or imaginary part could be used for further processing. To remove noise and acquisition angle dependent signal variations, a bandpass filter was then applied before combining the signals from all receiver coils to a single *SG* signal via *Principal Component Analysis (PCA)*. It was assumed that the variation of these profile-based *SG* signals reflect the respiratory motion, since different parts of the liver appear in the imaging *Field of View (FOV)* and the size of the lung changes. Together, these effects change the average signal intensity as measured via the k-space center or the projection data (*Inverse Fast Fourier Transform (IFFT)* of the k-space profiles).

In image-based *SG*, a sliding window reconstruction (see section 2.4) was performed. Manual placement of an image profile along the lung-liver interface yielded x-t data similar

to *Respiratory Navigator (RNAV)* measurements, and the *SG* signal was calculated by cross-correlation of the image profiles to a reference profile.

All *SG* variants were compared in 5 volunteers via visual inspection of image quality and quantitatively by evaluation of image sharpness relative to non-gated reconstructions. *CS* reconstruction (see section 2.3) was applied for reduction of artifacts in the undersampled data.

SG was then combined with *TPM* (see section 2.6) for the analysis of myocardial motion velocities (chapter 5). Image-based *SG* was used for this application, since it resulted in the maximal sharpness increase among the investigated variants. As 4 interleaved measurements were performed for *TPM* to obtain velocity information along all dimensions, less profile orientations could be covered at a given time. This resulted in higher undersampling for the sliding window reconstruction in the *SG* process, which could be compensated by *CS* reconstruction imposing a spatial smoothness constraint.

For *TPM* acquisition, blood suppression is usually applied to avoid inflow artifacts affecting the velocity measurements. In *SG-TPM*, the blood saturation slabs could be applied without restrictions, while the slabs had to be reduced in their thickness in the reference acquisition in order to avoid interference with the *RNAV* measurement. Additionally, the reference scan was prospectively *Electrocardiogram (ECG)*-triggered for defined *RNAV* measurement times, whereas the *SG* scan was retrospectively *ECG* synchronized, thus covering the whole cardiac cycle (see section 2.7).

CS reconstruction of the gated data was then performed and velocities were calculated. Different values of the temporal regularization strength (see section 2.3) were compared to investigate the influence on image and velocity information.

The study was performed in 10 volunteers and one patient, and the *SG-TPM* sequence was compared to the reference *RNAV-TPM* measurement. Visual image quality was graded according to a scale, and image sharpness and contrast were calculated. Velocity-time-curves (see section 2.6) were compared via peak analysis as well as correlation and *Root Mean Square Error (RMSE)* to the reference scan.

SG was then investigated for cardiac motion (chapter 6), where the temporal resolution to resolve the heartbeat is more demanding than for respiratory motion. Image-based *SG* in this application was calculated as the cross-correlation of an image *Region of Interest (ROI)* around the heart over time, based on a sliding window reconstruction. Peaks in the *SG* signal were used as a surrogate "R" peak (see section 2.7) for sorting the k-space data into heart phases within an average cardiac cycle. Reconstruction of the sorted data yielded a cine movie of the beating heart.

Sorting data acquired from multiple heartbeats into a single average cardiac cycle implicitly assumes uniform cardiac motion, i.e. no variation between different cycles. Although heartbeats with too much difference in beat duration are usually excluded from reconstruction, the assumption fails in case of cardiac arrhythmia, where strong variations of cycle durations occur. Thus, *SG* was extended to *Non-Uniform Self-Gating (nuSG)*, where no uniform motion was assumed. The method, like *SG*, was based on correlation of *ROI* data from a sliding window reconstruction. Instead of correlating with a single reference time frame, however, complete pair-wise correlation between all time frames was performed. Fitting "active contours" along the maxima in the resulting 2D correlation matrix found data similar to the respective motion state, while at the same time allowing continuous changes of motion pace by bending the fitting curves slightly. A "real-time" movie of the heart resolving every heartbeat separately rather than a single average beat could then be reconstructed, using all similar data from other hearbeats for increase of *Signal to Noise Ratio (SNR)*.

The study was performed in 3 patients with cardiac arrhythmia, and additionally in healthy volunteers and patients for imaging of the *Temporomandibular Joint (TMJ)* during mastication. Cardiac acquisitions were performed during a 6-second breathhold, i.e. no respiratory motion needed to be considered. Data were reconstructed with *CS* sliding window reconstruction, the *SG* as well as the *nuSG* method. Image data were compared regarding their image sharpness and the *Left Ventricle (LV)* blood pool area.

4 Comparison of Different Self-Gating Methods

This article [10] was published as

Paul, J., Divkovic, E., Wundrak, S., Bernhardt, P., Rottbauer, W., Neumann, H. and Rasche, V. (2015), High-resolution respiratory self-gated golden angle cardiac MRI: Comparison of self-gating methods in combination with k-t SPARSE SENSE. Magn Reson Med, 73: 292–298. doi: 10.1002/mrm.25102

and is © 2014 by Wiley Periodicals, Inc. Reprinted with permission.

High-Resolution Respiratory Self-Gated Golden Angle Cardiac MRI: Comparison of Self-Gating Methods in Combination with k-t SPARSE SENSE

Jan Paul,[1]* Evica Divkovic,[1] Stefan Wundrak,[1] Peter Bernhardt,[1] Wolfgang Rottbauer,[1] Heiko Neumann,[2] and Volker Rasche[1]

Purpose: To compare the applicability of different self-gating (SG) strategies for respiratory SG in cardiac MRI in combination with iteratively reconstructed (k-t SPARSE SENSE) cine data with low and high temporal resolution.

Methods: Eleven SG variants were compared in five volunteers by assessment of the resulting image sharpness compared with nongated reconstructions. Promising SG techniques were applied for high temporal resolution reconstructions of the heart function.

Results: SG was successful in all volunteers with image-based SG and the $\sum||p||$ technique. These approaches were also superior to gating from the respiratory bellows signal on average. Combination with k-t SPARSE SENSE enabled high temporally resolved visualization of the heart motion with free breathing.

Conclusion: Respiratory SG can be applied for improving image sharpness. Combining SG with iterative reconstruction allows generation of high temporal resolution cine data, which reveal more details of cardiac motion. **Magn Reson Med 73:292–298, 2015. © 2014 Wiley Periodicals, Inc.**

Key words: self-gating; golden angle radial acquisition; respiratory motion; cardiac MRI

INTRODUCTION

Cine cardiac MRI is used routinely for the assessment of functional parameters of the heart. For volumetric or flow acquisitions or when a high number of cardiac phases is required, the MRI data cannot be acquired within a single breath-hold of the patient and respiratory motion needs to be considered. The current standard comprises the application of respiratory navigators (RNAV) placed, for example, on the right hemidiaphragm to identify and to reject data acquired during respiratory motion phases (1–4). Because RNAV are only measured once or twice per heart cycle, respiratory motion within the cardiac cycle cannot be identified and is prone to yield motion artifacts. Alternative approaches such as self-gating (SG) often utilize the MRI data for identification of respiratory motion, thus enabling a more frequent, almost continuous sampling of the navigator signal.

Radial acquisition schemes enable extraction of the navigation data from the imaging data without any further modification of the MR sequence. Thus, no separate interleaved measurements prolong the scan or interrupt the steady-state condition. Furthermore, radial acquisition allows sliding window reconstruction of the data at different temporal and spatial resolutions, which even enables the use of low-resolution images instead of projections for SG without any time penalty. The golden angle acquisition order (5) places radial profiles in a way that every subset of contiguously acquired radial profiles covers 360° in an almost equal angular distribution, resulting in a better image quality of the sliding window reconstruction. In addition, the golden angle order results in a quasi-random profile order, which is a prerequisite for compressed sensing (6,7).

Different methods have been proposed to generate a SG signal. Some authors propose the use of the k-space center (8–13), whereas others rely on whole k-lines (8,14–23) or use reconstructed images (8,24). Different information in the data—magnitude (8–14,17,19–23), phase (8), real (12,15,16) or imaginary (12,16) part—were used as a source of the SG signal. Previous studies also allow reconstruction of cine images with high temporal resolution by utilization of motion correction (25) or prospective SG (21,22).

In this study, respiratory SG was combined with a golden angle radial data acquisition and a compressed sensing and parallel imaging technique [k-t radial SPARSE SENSE (6)] for the acquisition of cardiac cine images with a high number of cardiac phases. The different SG approaches were evaluated according to the resulting improvement in image sharpness, and the method was applied exemplarily to imaging of valve function.

METHODS

Study Protocol

Five healthy volunteers (age 25–28 y, all male) were enrolled for evaluation of the SG protocols. One further volunteer was enrolled for exemplary evaluation of the suggested technique. The study was approved by the

[1]Department of Internal Medicine II, University Hospital of Ulm, Ulm, Germany.

[2]Institute of Neural Information Processing, University of Ulm, Ulm, Germany.

Grant sponsor: Philips Healthcare.

*Correspondence to: Jan Paul, Department of Internal Medicine II, University Hospital of Ulm, Albert-Einstein-Allee 23, 89081 Ulm, Germany. E-mail: jan.paul@uniklinik-ulm.de

Additional Supporting Information may be found in the online version of this article.

Received 25 September 2013; revised 3 December 2013; accepted 6 December 2013

DOI 10.1002/mrm.25102

Published online 29 January 2014 in Wiley Online Library (wileyonlinelibrary.com).

© 2014 Wiley Periodicals, Inc.

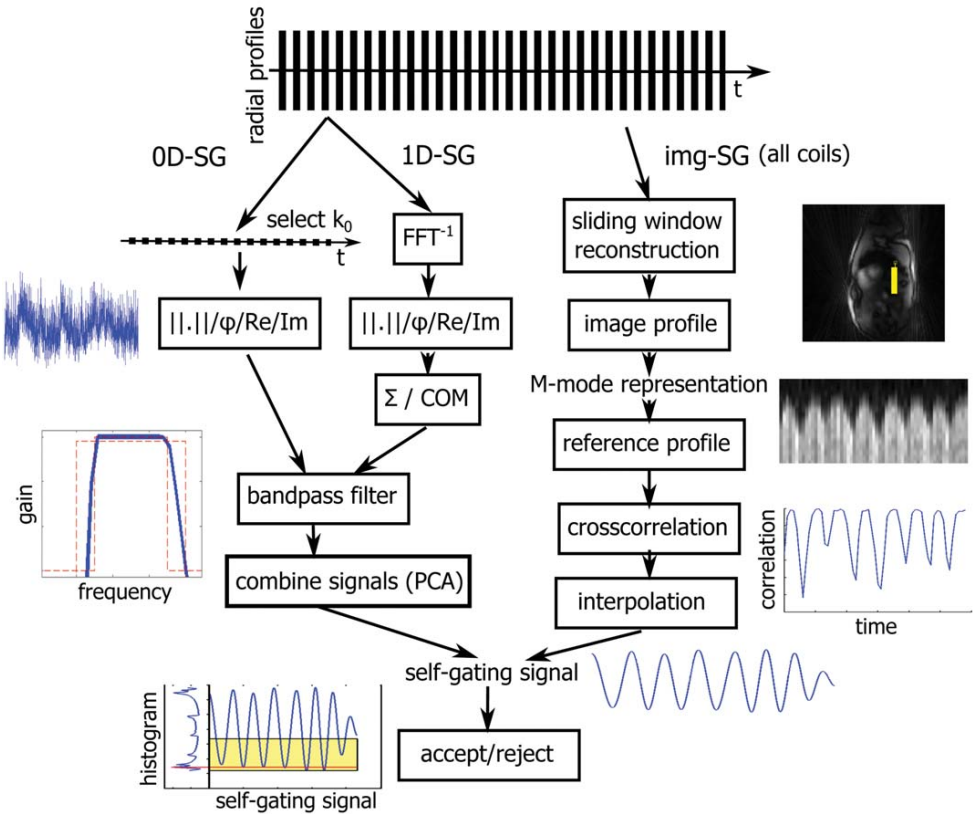

FIG. 1. Overview of the generation of different SG signals. 0D-SG uses the central value of each k-space profile, 1D-SG is based on the whole profiles, and img-SG depends on a sliding window reconstruction of the data. 0D-SG and 1D-SG signals are bandpass-filtered. Img-SG is generated by cross-correlation of a reference profile with the other image profiles. The SG signal is then used to accept or reject profiles prior to image reconstruction.

local ethics board and written informed consent was given by all volunteers prior to scanning.

MRI Protocol

For evaluation of the SG approaches, midventricular short-axis slices (SA) were acquired using a 3T whole-body MRI system (Achiva 3 T, Philips, Best, The Netherlands). All data were received using a 32-element cardiac coil. In total, 8600 radial profiles in golden angle acquisition geometry were acquired using a spoiled FLASH sequence within a 31-s scan time during free breathing of the volunteers. Acquisition parameters were as follows: echo time/repetition time = 1.31 ms/3.44 ms; field of view = 340 × 340 mm; slice thickness = 8 mm; resolution = 2 × 2 mm; flip angle $\alpha = 15°$; and pixel bandwidth p_ω = 862 Hz. Electrocardiography (ECG) and respiratory bellows data were recorded simultaneously with the data acquisition but not used for respiratory or cardiac synchronization during scanning.

As an exemplary clinical application, MRI data in three-chamber (3CH) geometry was acquired at 1.5T with a true fast imaging with steady state precession (FISP) sequence with $\alpha = 60°$, but otherwise similar acquisition to the one described above.

Self-Gating

After data acquisition, raw data were exported from the scanner and processed with MATLAB (MathWorks, Natick, Massachusetts, USA). Three types of SG techniques were compared (Fig. 1):

- zero-dimensional methods (0D-SG) depending on the k-space center, only,
- one-dimensional methods (1D-SG), in which a SG value is calculated from each radial projection p calculated as the 1D Fourier-transform over each single acquisition, and
- image-based SG (img-SG), in which a continuous RNAV-like signal is calculated from low-resolution images reconstructed by a sliding window technique.

Additionally, the respiratory bellows signal was used as a gating signal for comparison with the SG approaches.

0D-SG and 1D-SG

For 0D-SG, the central value k_0 after phase correction (26) of each k-space profile was selected for SG signal generation. Magnitude $||k_0||$, phase $\varphi(k_0)$, real $\Re(k_0)$, and imaginary $\Im(k_0)$ parts were analyzed.

1D-SG was calculated from 1D projections p of each radial acquisition. Magnitude ($||.||$), phase (φ), real ($\Re$), or imaginary ($\Im$) parts are used for either summation or calculation of the center of mass (COM), yielding $\sum||p||$, $\sum\varphi(p)$, and COM($||p||$), COM($\varphi(p)$), COM($\Re(p)$), COM ($\Im(p)$). Since mathematically $k_0 = \sum p$ and thus $\Re(k_0) = \Re(\sum p) = \sum\Re(p)$ and $\Im(k_0) = \Im(\sum p) = \sum\Im(p)$, the sum over the real and imaginary part were already considered as 0D-SG. COM was calculated in two dimensions from the profile and its two neighboring profiles by solving an overdetermined equation system in a least-square manner (8) and then projected on the axis of largest signal variation by principal component analysis (PCA) to get a 1D SG signal.

A Butterworth bandpass filter was applied to eliminate frequencies outside of the respiratory motion range, such as noise or angle-dependent signal variations. Passband was set to $f_{resp} \pm 0.05$ Hz, where f_{resp} was derived from the local maxima of the respiratory bellows signal. Stopband was set 0.05 Hz apart of the passband on both sides, and stopband attenuation was set to 30 dB.

Filtered SG signals from each coil element were combined by PCA over the coil dimension. Selection of the first component of the combined signals results in the SG signal exhibiting the largest amplitude.

Image-Based Self-Gating

Image-based SG is a semimanual method based on a sliding window reconstruction with a sliding window width and step size of 145 radial profiles, yielding a temporal resolution of ≈500 ms. Reconstruction was performed noniteratively from the central half of the radial profiles only, resulting in a two-fold reduced spatial resolution.

A line was placed manually on the liver–lung interface perpendicular to the diaphragm, similar to placing an RNAV for gated acquisitions. The 1D signal along this line was displayed over time. The highest liver position (corresponding to end-expiration) was automatically selected as a reference signal from the 1D signals by thresholding with the Otsu-method (27). Normalized cross-correlation between reference and the other 1D signals results in a value for each frame of the sliding window reconstruction. This signal was then interpolated to the total number of acquired radial profiles.

Bellows-Gating

For gating with the respiratory bellows, the signal was smoothed by a moving average filter of 145 points for noise reduction to ensure fair comparison with the img-SG approach.

Accept/Reject Data and Reconstruction

A histogram of the respiratory positions was obtained from each SG signal (Fig. 1). The acceptance window was placed symmetrically around the most frequent value (mode) of the histogram, spanning a range that leaves 20% of the data for reconstruction (fixed "navigator efficiency"). Using R-peak times as detected by the scanner software via ECG, the accepted radial profiles were sorted into phase bins that represent equally distributed cardiac phases over the whole cardiac cycle.

For the given acquisition parameters, the individual phase bins contain an insufficient number of radial profiles to meet the Nyquist sampling rate. Instead of increasing the acquisition time or decreasing the number of cardiac phases, parallel imaging [SENSE (28)] was combined with compressed sensing (7) for suppression of undersampling artifacts [k-t radial SPARSE SENSE (6)]. The sparsifying transformation ψ was set to the total variation along the temporal dimension. The objective function $f(x) = ||Ax - b||_2^2 + \lambda||\Psi x||_1$ was solved iteratively using a nonlinear conjugate gradient solver (7), where $A = GFS$ is the forward projection that combines the radial gridding operator G (29), Fourier transformation F, and coil sensitivity maps S. K-space phase bins are described as b, and x is the reconstructed image. The regularization parameter λ was tuned manually, but then held constant for all volunteers and SG approaches. For the reconstructions of 3CH data from 1.5T, regularization λ was tuned separately but held constant for all SG variants.

For each volunteer, cine data sets with cardiac phase intervals of 30 ms were reconstructed for each of the investigated SG schemes. After evaluation of the SG approaches, cine data sets with cardiac phase intervals of 10–18 ms were reconstructed applying the most promising SG technique. The acceptance window was increased to 40% for ensuring sufficient number of projections per bin.

Analysis

Image quality was assessed quantitatively by measuring image sharpness (30) defined as the average image gradient (calculated via 3 × 3 Sobel filters) in a rectangular region of interest (ROI) around the heart. Noise was removed from the gradient images by thresholding with the Otsu method (27) before averaging. This threshold was determined from nongated images and held fixed for gated reconstructions of the same volunteer. Image sharpness S_G of SG reconstructions was compared relatively with the sharpness S_{NG} of nongated reconstructions according to $S_{rel} = \frac{S_G - S_{NG}}{S_{NG}} \cdot 100$ [%]. M-mode–like presentations of the cardiac motion were compared visually for the reconstructions with low and high temporal resolution.

RESULTS

The MRI examination could be finished in all volunteers. The detected respiratory frequencies f_{resp} used for bandpass filtering were in the range of 0.21–0.32 Hz (≈13–19 min^{-1}). Average undersampling factors were R = 5.2 ± 1.6 for 30 ms cardiac phase interval with 20% navigator efficiency and R = 8.2 ± 0.3 for 10 ms cardiac phase interval and 40% navigator efficiency.

SG signals for all SG variants in two volunteers are provided in Figure 2, and quantitative assessment of the improvement of the image sharpness resulting for the different SG approaches is shown in Figure 3. The SG signals COM($\varphi(p)$), COM($\Re(p)$), and COM($\Im(p)$) show degradation that result in inferior image quality as

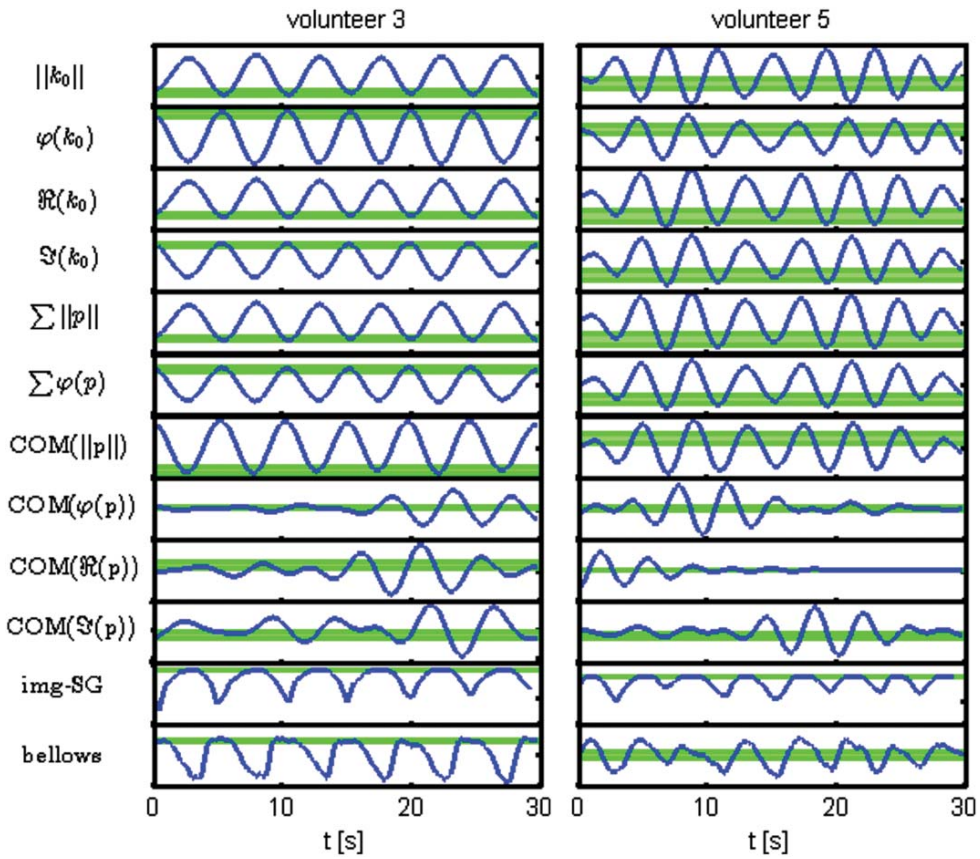

FIG. 2. SG signals with the acceptance windows for 20% navigator efficiency for all variants and two volunteers, in different arbitrary units. Note that the automatic placement of the gating window may cause strong differences in the accepted profiles even if only tiny differences are apparent in the gating signals [e.g., COM($\varphi(p)$) versus COM($\Re(p)$) or $\sum||p||$ versus $\sum\varphi(p)$ in volunteer 5].

measured by the investigated image sharpness criteria. 0D-SG and 1D-SG reveal no tendency regarding which part of the signal (magnitude, phase, real, or imaginary part) generally results in better image sharpness. Image-based SG and the $\sum||p||$ technique as well as reconstructions from bellows-gating improved image sharpness for all volunteers, and img-SG was the best approach on average. While bellows-gating is clearly inferior to img-SG, the sharpness improvement of 0D-SG and 1D-SG (except for three COM-based techniques) yields comparable average results. Representative images obtained with and without SG and with bellows-gating are shown in Figure 4 (see Supporting Information for the respective videos of the cine reconstructions).

Visual assessment of the resulting image sharpness (Fig. 4) confirms the quantitative assessment. Although clear image blur caused by respiratory motion can be appreciated for nongated and COM-based reconstructions, bellows-gated reconstruction appears sharper at the LV myocardium, whereas image-based SG shows almost complete elimination of the motion blur.

A direct comparison of SA and 3CH views reconstructed with long and short cardiac phase interval is shown in Figure 5. The M-modes clearly show the improved temporal resolution of the reconstructions with short cardiac phase interval. Where the papillary muscle in the SA and the mitral valve in the 3CH view are blurred in the long cardiac phase interval reconstructions, a much clearer delineation of the structures can be appreciated in the high cardiac phase interval reconstructions. In SA, motion of the papillary muscle (black arrows) is continuous in the reconstruction with a short

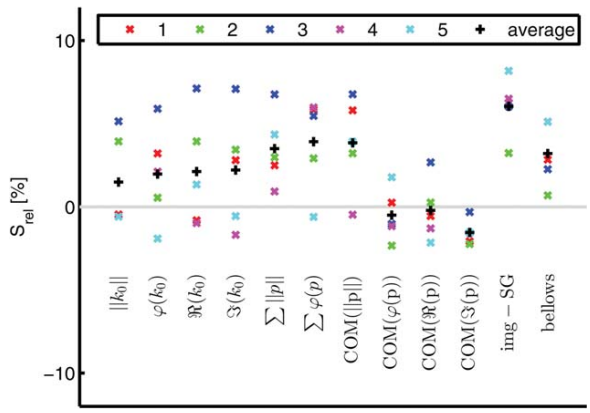

FIG. 3. Comparison of increase in image sharpness compared with nongated reconstruction for the different SG variants. Data are shown for individual volunteers (×) and as average (+).

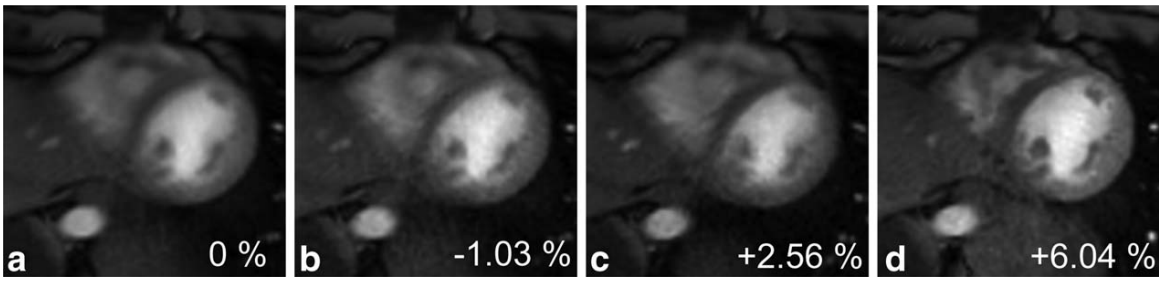

FIG. 4. Example images of nongated and gated reconstructions. Nongated (**a**) and COM($\varphi(p)$) gated (**b**) reconstructions are blurred, especially at the septal wall. Bellows-gated reconstruction (**c**) is slightly improved compared with panels a and b, and the reconstruction from img-SG (**d**) is almost free of motion artifacts. Increase of image sharpness relative to non-gated sharpness is indicated for each reconstruction. Cine reconstructions for all SG variants in one volunteer are available in the Supporting Information.

cardiac phase interval, whereas an abrupt change of position appears in the M-mode of a long cardiac phase interval. Especially for the mitral valve in 3CH, the reconstruction with a short cardiac phase interval enables the delineation of the valve (white arrow) from the flow induced signal variations (asterisk).

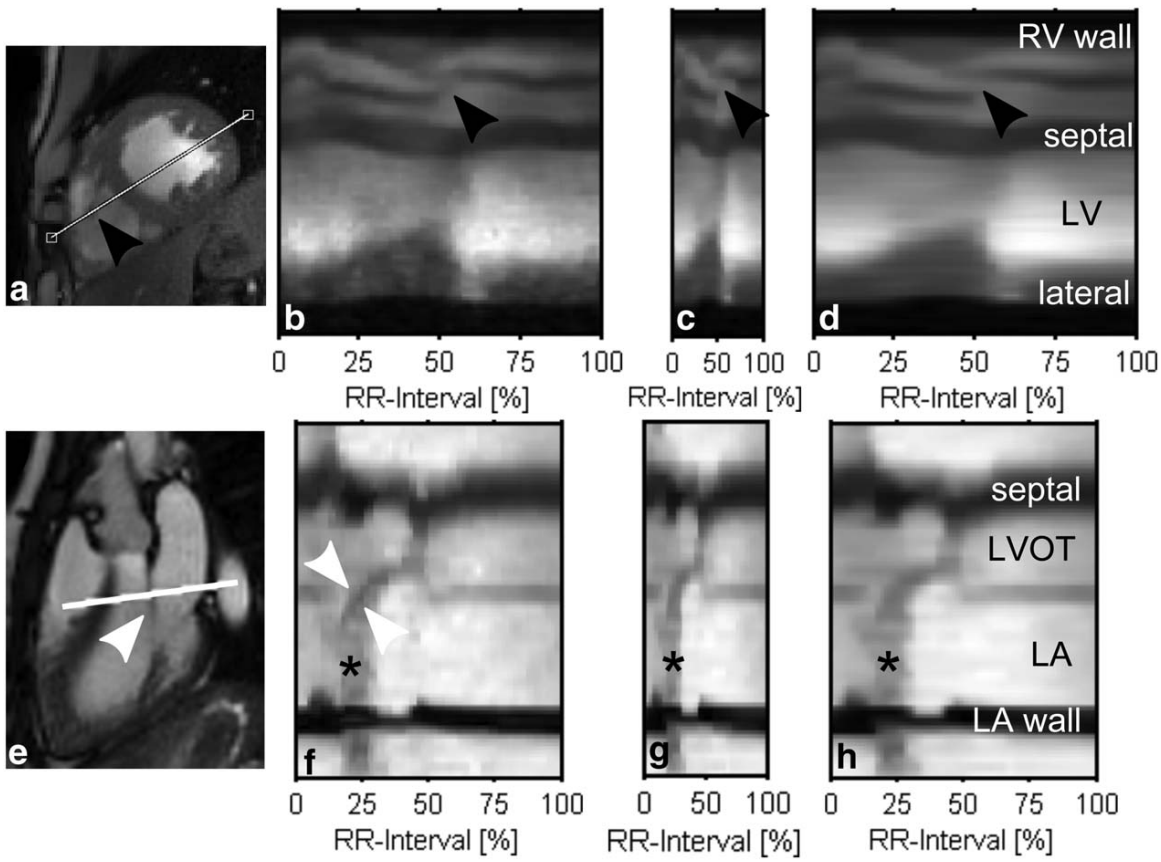

FIG. 5. Example of M-mode–like presentation of gated reconstructions (img-SG) for a long and short cardiac phase interval in SA (**a–d**) and 3CH (**e–h**) view. Placement of the profiles is shown in panels a and e. In the SA view, motion of the papillary muscle (black arrowheads) is depicted continuously for the short cardiac phase interval (b), whereas abrupt change of position appears in reconstruction from the long cardiac phase interval (c) or its temporal interpolation (d). In 3CH view, the mitral valve appears with more defined edges in short cardiac phase interval reconstruction (f) while being blurred in the reconstruction with the long cardiac phase interval (g) or its temporal interpolation (h). Also, at approximately 20%–25 % of the RR interval, blood-flow artifacts from the left ventricular outflow tract reach the left atrium. While the mitral valve is darker (white arrowhead) than the artifacts (asterisk) and can be distinguished in panel f, valve and artifacts appear as a single blurred structure in panels g and h. The Supporting Information provides videos of the 3CH view. Abbreviations: LA, left atrium; LV, left ventricle; LVOT, left ventricular outflow tract; RV, right ventricle.

DISCUSSION

Respiratory SG was combined with parallel compressed sensing for providing functional information of the heart with phase intervals as short as 10 ms. Different respiratory SG methods were compared via an increase in image sharpness relative to nongated reconstructions. A high intervolunteer variance could be observed even within this small study population, and only img-SG, $\sum||p||$, and bellows-gated reconstructions yielded image sharpness improvements in all cases. Larson et al. (8) found no significant difference in magnitude-based 0D-SG, 1D-SG, and img-SG (img-SG using cross-correlation) when used for cardiac SG by assessing the SG quality via variation from ECG trigger and expert image score. Spincemaille et al. (12) used magnitude, real or imaginary part of 0D-SG and selected the variant via maximal correlation with RNAV during a calibration scan, but did not state statistics of the selection in their study.

For 0D-SG, often several echo peaks are sampled and the maximum or average is taken to overcome acquisition imperfections and to be sure to include k_0 (10,11). In the work presented here, correction of shifted k-space data by removing linear phase errors of the radial profiles (26) renders this unnecessary.

0D-SG and 1D-SG implicitly assume a sinusoidal respiratory motion, as the bandpass filter removes all frequencies except a very small range. A fixed passband range of 0.1–0.5 Hz as in (11) was also tested but resulted in the same ranges of increase in image sharpness, while more oscillations occurred in the SG signals. Image-based SG, however, can cope with variations of respiratory motion, such as hysteresis, due to signal generation via cross-correlation. Generation of the img-SG signal is based on a sliding window reconstruction, thus averaging data of 145 profiles, which is similar to a lowpass filter. Application of a lowpass filter instead of a bandpass filter however is not sufficient for 0D-SG and 1D-SG, since low-frequency modulations remain in the signal. Spincemaille et al. (12) use a sinusoidal Kalman filter model to remove signal parts not related to respiratory motion.

To avoid the need of recording the bellows signal, detection of the individual respiratory frequency f_{resp} is also possible for $\sum||p||$ by selecting the peak frequency of the SG signal in the range of 0.1–0.5 Hz after Gaussian weighting of the frequency spectrum in this range (with maximum difference of 0.026 Hz to f_{resp} as detected from bellows).

Instead of combining SG signals of all coils, other authors automatically select a single coil element for generation of 0D-SG or 1D-SG, based on a measure, such as the minimal standard deviation of cycle times (9,11,19), maximum signal amplitude (10), most occurring end-expiratory positions calculated as SG signal values above 80% of maximum SG value (11), or correlation of the SG signal with RNAV or bellows signals (12). Selection of a specific coil element could be useful to suppress signal variations not related to respiratory motion even before application of a bandpass filter.

While 0D-SG and 1D-SG require no manual user interaction, an image profile has to be placed for img-SG. Utilizing a graphical user interface allows optimization of the img-SG signal by adjusting the profile position and immediately assessing the SG signal visually.

SG in combination with parallel imaging and compressed sensing allows reconstruction of highly undersampled cardiac phase bins up to an average undersampling factor of R = 8, to increase the temporal resolution of cine data.

SG depends on the acquired imaging data by principle. Thus, quality of the SG signal can change with modifications of acquisition parameters, such as image contrast or usage of blood suppression techniques. Also, slice orientation can influence the SG signal, since different portions of the liver are imaged for different angulations. Brau and Brittain (10) found the largest 0D-SG signal variation for liver imaging in axial slice orientation, due to the most through-plane motion of the liver, compared with sagittal and coronal slices. However, SG was successful for SA and 3CH view and using a FLASH or true FISP sequence in this study. Further investigation is needed to evaluate the SG approaches for other slice orientations or volumetric acquisition, and different sequences such as flow-encoding acquisition.

CONCLUSIONS

Respiratory SG can improve image sharpness relative to nongated reconstruction. Image-based SG and 1D-SG using the sum of magnitude succeeded in all investigated cases and were superior to bellows-gating on average.

Combination of radial golden angle acquisition with SG and an iterative reconstruction algorithm allows reconstruction of highly undersampled data, thus enabling the generation of high temporal resolution cine data revealing more details of cardiac motion.

REFERENCES

1. Firmin D, Keegan J. Navigator echoes in cardiac magnetic resonance. J Cardiovasc Magn Reson 2001;3:183–193.
2. Jung B, Zaitsev M, Hennig J, Markl M. Navigator gated high temporal resolution tissue phase mapping of myocardial motion. Magn Reson Med 2006;55:937–942.
3. Peters DC, Nezafat R, Eggers H, Stehning C, Manning WJ. 2D free-breathing dual navigator-gated cardiac function validated against the 2D breath-hold acquisition. J Magn Reson Imaging 2008;28: 773–777.
4. Abd-Elmoniem KZ, Obele CC, Sibley CT, Matta JR, Pettigrew RI, Gharib AM. Free-breathing single navigator gated cine cardiac magnetic resonance at 3 T: feasibility study in patients. J Comput Assist Tomogr 2011;35:382–386.
5. Winkelmann S, Schaeffter T, Koehler T, Eggers H, Doessel O. An optimal radial profile order based on the golden ratio for time-resolved MRI. IEEE Trans Med Imaging 2007;26:68–76.
6. Feng L, Chandarana H, Xu J, Block KT, Sodickson D, Otazo R. K-t radial SPARSE-SENSE: combination of compressed sensing and parallel imaging with golden angle radial sampling for highly accelerated volumetric dynamic MRI. In Proceedings of the 20th Annual Meeting of ISMRM, Melbourne, Australia, 2012. p. 81.
7. Lustig M, Donoho DL, Santos JM, Pauly JM. Compressed sensing MRI. IEEE Signal Processing Magazine 2008;25:72–82.
8. Larson AC, White RD, Laub G, McVeigh ER, Li D, Simonetti OP. Self-gated cardiac cine MRI. Magn Reson Med 2004;51:93–102.
9. Crowe ME, Larson AC, Zhang Q, Carr J, White RD, Li D, Simonetti OP. Automated rectilinear self-gated cardiac cine imaging. Magn Reson Med 2004;52:782–788.

10. Brau ACS, Brittain JH. Generalized self-navigated motion detection technique: Preliminary investigation in abdominal imaging. Magn Reson Med 2006;55:263–270.
11. Buehrer M, Curcic J, Boesiger P, Kozerke S. Prospective self-gating for simultaneous compensation of cardiac and respiratory motion. Magn Reson Med 2008;60:683–690.
12. Spincemaille P, Nguyen TD, Prince MR, Wang Y. Kalman filtering for real-time navigator processing. Magn Reson Med 2008;60:158–168.
13. Manka R, Buehrer M, Boesiger P, Fleck E, Kozerke S. Performance of simultaneous cardiac-respiratory self-gated three-dimensional MR imaging of the heart: initial experience. Radiology 2010;255:909–916.
14. Kim WS, Mun CW, Kim DJ, Cho ZH. Extraction of cardiac and respiratory motion cycles by use of projection data and its applications to NMR imaging. Magn Reson Med 1990;13:25–37.
15. Spraggins TA. Wireless retrospective gating: application to cine cardiac imaging. Magn Reson Imaging 1990;8:675–681.
16. White RD, Paschal CB, Clampitt ME, Spraggins TA, Lenz GW. Electrocardiograph-independent,"wireless" cardiovascular cine MR imaging. J Magn Reson Imaging 1991;1:347–355.
17. Lai P, Larson AC, Bi X, Jerecic R, Li D. A dual-projection respiratory self-gating technique for whole-heart coronary MRA. J Magn Reson Imaging 2008;28:612–620.
18. Stehning C, Börnert P, Nehrke K, Eggers H, Stuber M. Free-breathing whole-heart coronary MRA with 3D radial SSFP and self-navigated image reconstruction. Magn Reson Med 2005;54:476–480.
19. Liu J, Spincemaille P, Codella NCF, Nguyen TD, Prince MR, Wang Y. Respiratory and cardiac self-gated free-breathing cardiac CINE imaging with multiecho 3D hybrid radial SSFP acquisition. Magn Reson Med 2010;63:1230–1237.
20. Uribe S, Beerbaum P, Sørensen TS, Rasmusson A, Razavi R, Schaeffter T. Four-dimensional (4D) flow of the whole heart and great vessels using real-time respiratory self-gating. Magn Reson Med 2009; 62:984–992.
21. Uribe S, Tejos C, Razavi R, Schaeffter T. New respiratory gating technique for whole heart cine imaging: integration of a navigator slice in steady state free precession sequences. J Magn Reson Imaging 2011; 34:211–219.
22. Uribe S, Muthurangu V, Boubertakh R, Schaeffter T, Razavi R, Hill DLG, Hansen MS. Whole-heart cine MRI using real-time respiratory self-gating. Magn Reson Med 2007;57:606–613.
23. Spincemaille P, Liu J, Nguyen T, Prince MR, Wang Y. Z intensity-weighted position self-respiratory gating method for free-breathing 3D cardiac CINE imaging. Magn Reson Imaging 2011;29:861–868.
24. Larson AC, Kellman P, Arai A, Hirsch GA, McVeigh E, Li D, Simonetti OP. Preliminary investigation of respiratory self-gating for free-breathing segmented cine MRI. Magn Reson Med 2005;53:159–168.
25. Hansen MS, Sørensen TS, Arai AE, Kellman P. Retrospective reconstruction of high temporal resolution cine images from real-time MRI using iterative motion correction. Magn Reson Med 2012;68:741–750.
26. Rasche V, Holz D, Proska R. MR Fluoroscopy using projection reconstruction multi-gradient-echo (prMGE) MRI. Magn Reson Med 1999; 42:324–334.
27. Otsu N. A threshold selection method from gray-level histograms. IEEE Trans Sys, Man, Cyber 1979;9:62–66.
28. Pruessmann KP, Weiger M, Scheidegger MB, Boesiger P. SENSE: sensitivity encoding for fast MRI. Magn Reson Med 1999;42:952–962.
29. Rasche V, Proksa R, Sinkus R, Bornert P, Eggers H. Resampling of data between arbitrary grids using convolution interpolation. IEEE Trans Med Imaging 1999;18:385–392.
30. McGee KP, Manduca A, Felmlee JP, Riederer SJ, Ehman RL. Image metric-based correction (Autocorrection) of motion effects: analysis of image metrics. J Magn Reson Imaging 2000;11:174–181.

5 Combination of Respiratory Self-Gating and Tissue Phase Mapping

This article [11] was published as

Paul, J., Wundrak, S., Bernhardt, P., Rottbauer, W., Neumann, H. and Rasche, V. (2015), Self-Gated Tissue Phase Mapping using Golden Angle Radial Sparse SENSE. Magn Reson Med. doi: 10.1002/mrm.25669

and is © 2015 by Wiley Periodicals, Inc. Reprinted with permission.

FULL PAPER

Magnetic Resonance in Medicine 00:00–00 (2015)

Self-Gated Tissue Phase Mapping Using Golden Angle Radial Sparse SENSE

Jan Paul,[1]* Stefan Wundrak,[1] Peter Bernhardt,[1] Wolfgang Rottbauer,[1] Heiko Neumann,[2] and Volker Rasche[1]

Purpose: To investigate the combination of Golden Angle Radial Sparse SENSE reconstruction with image-based self-gating (SG) for deriving high-quality TPM data from radial golden angle (GA) k-space data.

Methods: In 10 healthy volunteers, a self-gated radial GA TPM sequence (TPM_{SG}) was compared with a prospectively triggered radial TPM acquisition with conventional respiratory (RNAV) compensation (TPM_{ref}). Image quality and velocities were compared for different regularization strengths λ in the CS reconstruction.

Results: Acquisitions and retrospective self-gating was successful in all cases. Contrast in TPM_{SG} was superior to TPM_{ref}, because the blood saturation bands could be applied with full thickness without interference with the RNAV. Velocities from both acquisitions visually showed the same motion patterns and were quantitatively highly similar (correlation 0.81–0.97 and RMSE 0.08–0.21 cm/s). Strong temporal regularization ($\lambda \in \{0.3, 0.4\}$) led to reduced velocity peaks in TPM_{SG}. For $\lambda = 0.2$, image sharpness as well as velocity peaks of TPM_{SG} were comparable to TPM_{Ref}.

Conclusion: The combination of Golden Angle Radial Sparse SENSE with image-based self-gating allows measurement of velocities of the myocardium with superior black-blood contrast and full coverage of the cardiac cycle. **Magn Reson Med 000:000–000, 2015. © 2015 Wiley Periodicals, Inc.**

Key words: self-gating; tissue phase mapping (TPM); golden angle; cardiac MRI

INTRODUCTION

Global and regional myocardial motion quantification appears mandatory for detailed understanding of contraction abnormalities in cardiac pathologies (1,2) and may facilitate better diagnosis as well as treatment selection and planning. MRI has turned out as a reproducible tool for global and regional wall motion properties assessment. For the quantification of motion abnormalities a variety of velocity- and strain-based parameters have been investigated (3), clearly indicating the potential for separation of different diseases. In contrast to other techniques (4–7), tissue phase mapping (TPM) (8) appears promising because it generates highly precise and reproducible (9) three-dimensional information, does not require complex postprocessing and can be applied to analyze the entire cardiac cycle (10). However, its clinical usage is limited by the rather long acquisition times.

Even though different acceleration techniques led to a reduction of scan times (11–13), respiratory motion has still to be considered a critical limitation for high spatiotemporal resolution or volumetric TPM acquisitions.

The traditional approach of respiratory gating with pencil beam navigators (RNAVs) has major disadvantages. The acquisition has to be interrupted for the RNAV measurement, thus prolonging the acquisition time and interrupting the steady state. Only prospective cardiac triggering is possible for defined acquisition of the RNAV signal, and the RNAV is only measured once or twice per heart beat and cannot accommodate motion between these measurements. Self-gating (SG) however provides an almost continuous respiration signal from the imaging data itself (14,15) and allows retrospective choice of parameters like acceptance window width or "navigator efficiency." The radial golden angle acquisition scheme (16) enables sliding window reconstruction of different window widths and temporal resolutions, which can be used for generation of the SG signal (17).

Additionally, the golden angle acquisition order generates a quasirandom distribution of radial profiles which leads to a temporal incoherent sampling scheme that can be exploited by compressed sensing reconstruction (18,19), which takes into account the expected sparseness of the measured signal and is in particular effective if signal sparsity in the temporal domain is exploited (20–22). To achieve the necessary temporal resolution, the k-space for a single acquired time frame is undersampled, which leads to an underdetermined reconstruction problem with many solutions. Spatial and/or temporal regularization is used to give preference to a particular sparse solution. In case of compressed sensing, the ℓ_1-norm in combination with a sparsifying transform is used for regularization. Feng et al. recently introduced Golden Angle Radial Sparse SENSE using the temporal total variation transform as the sparsifying transformation and were able, in combination with parallel imaging, to reconstruct dynamic cardiac images from as low as 21 radial profiles per frame (23). Compressed sensing reconstruction promises a shortened acquisition time for TPM by achieving the same spatiotemporal resolution from fewer k-space profiles, which seems especially promising in respect to the four-fold prolonged acquisition time to acquire the necessary velocity encoded images.

[1]Department of Internal Medicine II, University Hospital of Ulm, Germany.
[2]Institute of Neural Information Processing, University of Ulm, Germany.
*Correspondence to: Jan Paul, Dipl.-Inf., Department of Internal Medicine II, University Hospital of Ulm, Albert-Einstein-Allee 23, 89081 Ulm, Germany. E-mail: jan.paul@uniklinik-ulm.de

Received 25 August 2014; revised 13 January 2015; accepted 2 February 2015
DOI 10.1002/mrm.25669
Published online 00 Month 2015 in Wiley Online Library (wileyonlinelibrary.com).

© 2015 Wiley Periodicals, Inc.

Table 1
Parameters for the Investigated Prospective (TPM_{ref}) and Self-Gated (TPM_{SG}) Tissue Phase Mapping Protocols

Parameter	TPM_{ref}	TPM_{SG}
Scanner model	Philips Achieva 3T (Best, The Netherlands)	
Receive coil	32-element cardiac coil	
TR/TE	5.3 ms/3.2 ms	5.6 ms/3.4 ms
Flip angle	15°	
Flow measurement	4-point balanced (Hadamard) (38) Encoding direction changed every heartbeat	4-point balanced (Hadamard) (38) Encoding direction changed every repetition
VENC	30 cm/s in all three directions	
Blood suppression	Alternating saturation slab (24) Every 3rd repetition Width: 20–45 mm Flip angle: 90°	Alternating saturation slab (24) Every 4th repetition Width: 60 mm Flip angle: 90°
FOV	340 mm x 340 mm	
Slice thickness	8 mm	
Readout points per radial profile	172	228
Reconstructed resolution	2 mm x 2 mm	
Temporal resolution	23 ms	23 ms (retrospective)
Cardiac synchronization	ECG, prospective	ECG, retrospective
Respiratory motion compensation	Pencil beam navigator (RNAV) 8 mm acceptance window	retrospective self-gating 8 mm acceptance window
Scan duration per slice	2 min 57 s (nominal) 4 min 48 s ± 18 s (navigator efficiency taken into account)	5 min 40 s (acquired) 4 min 48 s (data used for reconstruction)
Undersampling	R = 2	Dependent on retrospective navigator efficiency

Recently, first approaches combining TPM and retrospective cardiac triggering for full coverage of the cardiac cycle have been published (9,15).

The objective of this study was to investigate the combination of a Golden Angle Radial Sparse SENSE reconstruction technique with image-based self-gating for deriving high-quality TPM data from radial golden angle k-space data.

METHODS

Study Population

Ten healthy volunteers (7 male, 3 female, aged 31 ± 10 years) and one patient (68 years, male, cardiomyopathy, reduced LV function) were investigated. The study was approved by the local ethics committee and written informed consent was obtained prior to the examination.

Acquisition

Radial TPM acquisitions were performed in three short axis views, located at approximately 25% (basal), 50% (mid-ventricular), and 75% (apical) of the left ventricle (LV) identified along the long axis in the systolic two-chamber and four-chamber views. Each volunteer underwent two radial TPM acquisitions. A prospectively triggered radial TPM acquisition with conventional RNAV respiratory compensation as reference (TPM_{ref}) and a self-gated golden angle TPM sequence (TPM_{SG}). For both scans, black-blood contrast was generated by applying saturation bands on either side of the slices. For SAR constraints and minimization of black-blood preparation time, the saturation bands were applied alternating before subsequent TPM acquisition blocks (24). Saturation band widths were chosen as closely as possible to 60 mm. However, to avoid interferences of the saturation bands with the RNAV, the saturation band thickness had to be reduced for TPM_{ref}. In TPM_{ref} the velocity encoding direction was changed after each heart beat and three radial k-space lines (3 TR) were encoded after each saturation preparation, where for TPM_{SG} the velocity encoding direction was changed every repetition and a single k-space profile was encoded for all velocity directions (4 TR) between subsequent saturation preparations. Undersampling was set to R = 2 (132 radial profiles per cardiac phase) with respect to the radial Nyquist theorem in TPM_{ref} resulting in an acquisition time of 2 min 57 s per slice (for 100% navigator efficiency). In TPM_{SG}, data were sampled continuously for 5 min 40 s, matching the acquisition time of TPM_{ref} for assumed 50% navigator efficiency, and the undersampling factors resulted from the retrospective gating efficiency. The volunteers' ECG was recorded simultaneously for enabling full retrospective ECG triggering in TPM_{SG}. Detailed acquisition parameters are provided in Table 1.

Data Reconstruction

All raw data were exported from the scanner and further processed and reconstructed in Matlab (Mathworks, Natick, MA). Coil sensitivity maps were estimated using a separate coil calibration scan and an iterative estimation method that was regularized using the ℓ_2-norm of the finite difference of the coil sensitivities to promote smoothness of the maps (25,26).

For TPM_{SG}, the self-gating signal was generated from images reconstructed by a sliding window reconstruction from the golden angle data as suggested earlier (17).

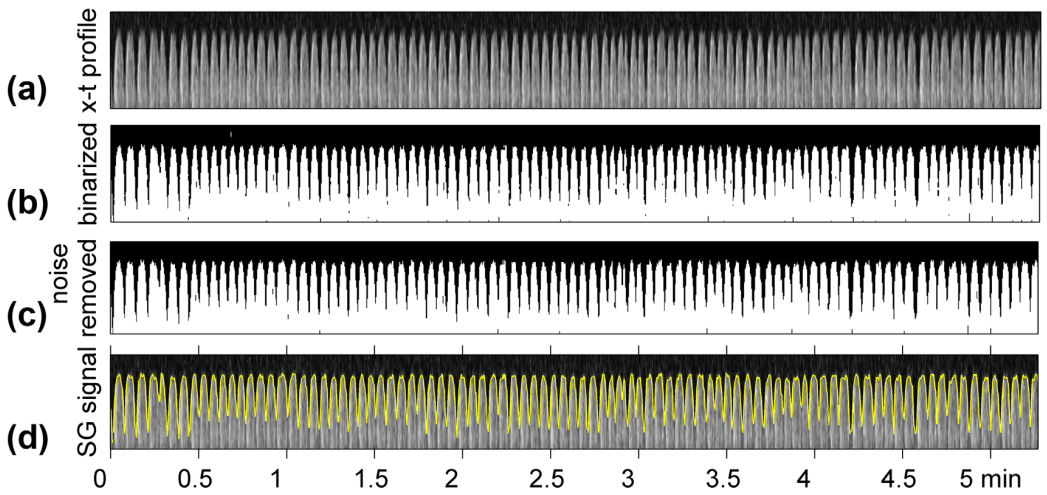

FIG. 1. Calculation of the self-gating (SG) signal: The x-t image (**a**) from a profile across the lung-liver interface is converted to a binary image (**b**) by means of an automatically determined threshold, noise is removed in the lung (black) and liver (white) area (**c**), and the SG signal is determined as the highest liver position at each time point (**d**).

Because three-dimensional velocity encoding demands four measurements of each profile before advancing to the subsequent profile with golden angle angular spacing, the reconstruction window was prolonged to 500 ms (18 radial profiles per frame) to ensure sufficient image quality in the resulting sliding window images. The sliding window was shifted by nine radial profiles to yield a frame every 250 ms. Reconstruction was performed using Golden Angle Radial Sparse SENSE with spatial but no temporal total variation regularization to avoid any impact on the temporal fidelity of the gating data. After interactive placement of a line at the lung-liver interface, an x-t image (similar to a conventional RNAV) was generated by plotting the intensity profiles along the line over time (Fig. 1a). The x-t image was binarized (Fig. 1b) using an automatically calculated threshold (27), and noise was removed by application of the morphological image operations "opening" and "closing" provided in Matlab (Fig. 1c). The liver position was then determined from this image for each frame (Fig. 1d) and interpolated to yield an SG signal for each radial profile.

The acceptance window was set to 8 mm and placed automatically around the end-expiratory position, which was assumed the most frequently occurring respiratory position as determined by means of histogram analysis. The number b of histogram bins was calculated automatically according to $b = \lceil \frac{max(p)-min(p)}{w} \rceil$ as suggested in Freedman and Diaconis (28) by means of the bin width $w = 2 \cdot IQR(p) \cdot n^{-1/3}$, where $IQR(p)$ is the interquartile range of the respiratory positions p and n is the total number of radial profiles.

Retrospective cardiac synchronization was achieved applying the recorded ECG and data were sorted into cardiac phase bins with a temporal resolution of 23 ms similar to the cardiac phase resolution in the reference scan. Data used for reconstruction were restricted to the data acquired in the same scan time as TPM_{Ref} including navigator efficiency (see also the Results section).

Compressed sensing reconstruction of the TPM_{SG} data was performed for each velocity encoding direction separately by Golden Angle Radial Sparse SENSE (17,23,29) minimizing the objective function $f(x) = ||Ax - b||_2^2 + \lambda||\Lambda\nabla_t x||_1$. A nonlinear conjugate gradient solver (19) was applied, where the forward operator $A = GFS$ combined gridding G (30), Fourier transformation F, and coil sensitivity maps S. The ℓ_2-norm enforces data consistency between the k-space b and the reconstructed image x. ∇_t denotes the gradient operator along the temporal dimension (which is approximated by a finite backward difference kernel). The combination of ∇_t with the ℓ_1-norm forms the total variation (TV) regularization, which exploits sparsity of $\nabla_t x$ by assuming a piecewise constant signal function for each pixel over time (22), resulting in most coefficients of $\nabla_t x$ to be zero. This assumption can be justified, because the continuous motion (in-plane and through-plane) of an approximately spatially piecewise constant image yields a piecewise constant signal function for each pixel over time. For improved suppression of undersampling artifacts, the regularization was spatially adapted by the diagonal matrix $\Lambda\epsilon[0,1]^{n\times n}$ as described in Wundrak et al (29) based on an estimation of the level of undersampling artifacts of the gridding solution using the temporal total variation of the noniterative gridding solution $diag(\Lambda) = ||\nabla_t\ A^H b||_1$. The objective function was solved approximately using corner rounding (i.e., the approximation $|x| \approx \sqrt{x^* x + \varepsilon}$ with $\varepsilon = 10^{-4}$) for the gradient calculation of the l_1-term and an inexact backtracking line search using the Armijo rule ($c = 0.05$) in combination with the method of Hager and Zhang (31,32). The system was left preconditioned using the square root of the k-space sampling density function to speed up convergence and the solver was terminated after 15 iterations in all cases. No method to enforce convergence was applied. The regularization parameter λ was held

constant. We investigated the impact of the temporal regularization on the velocity data fidelity by using values of $\lambda \in \{0.1, 0.2, 0.3, 0.4\}$. No additional regularization in the spatial domain was applied. The k-space data were normalized to a fixed ℓ_2-norm of 100 per frame before reconstruction for comparability of different choices of λ.

The TPM_{ref} data were directly reconstructed by applying a gridding technique without further iteration or regularization, because image quality was sufficient due to the rather low undersampling factor of $R = 2$ (132 radial profiles per frame).

Data Analysis

Velocities along the three main axes were calculated from the independently reconstructed Hadamard velocity-encoded images for TPM_{ref} and TPM_{SG}. Background errors of the velocities were corrected by subtracting a plane fitted through the velocities of stationary tissue (33). A mask $\mu(r,t)$ for the myocardium was generated semiautomatically for all cardiac phases. Based on manual contouring of the epi- and endocardial borders in two cardiac phases the contours were automatically tracked for all other cardiac phases (34,35). Before further processing, all endo- and epicardial contours were checked and manually redefined in case of segmentation errors. Radial (contraction–expansion), circumferential (rotation), and longitudinal (through-plane) velocities were calculated for all pixels within the segmented myocardium.

Quality of magnitude images as well as velocities were compared between TPM_{Ref} and TPM_{SG} for different values of λ.

Image quality was determined by scoring of the cine data by consensus of two experienced observers blinded to the acquisition and reconstruction method according to the 5-point scheme described in (15): 1, poor (segmentation impossible); 2, fair (difficult segmentation); 3, acceptable (segmentation possible for experienced observer); 4, good (segmentation possible for inexperienced observer); 5, excellent (trivial segmentation).

The inverse of the coefficient of variation for magnitude (CV_M^{-1}) and velocities (CV_V^{-1}) were estimated from maps calculated as the mean value divided by the standard deviation in a 5×5 mask, from which the average within the myocardium at the peak of the longitudinal S wave was taken.

Edge sharpness was measured as the inverse of the distance of the 20% and 80% level of an image profile (36). Sharpness was evaluated from profiles along the LV border and averaged over all cardiac phases.

Myocardium-to-blood contrast was determined as $C = \frac{|M-B|}{M+B}$, where M is the average image intensity on the myocardium and B the average image intensity in the blood pool. This value was evaluated at the S peak of the longitudinal velocity.

Velocities were compared by the amplitudes and times of radial and longitudinal S, E, and A velocity peaks, and segmental velocities from 24 segments per slice were compared by mean correlation, root-mean-square error (RMSE), and residual displacement

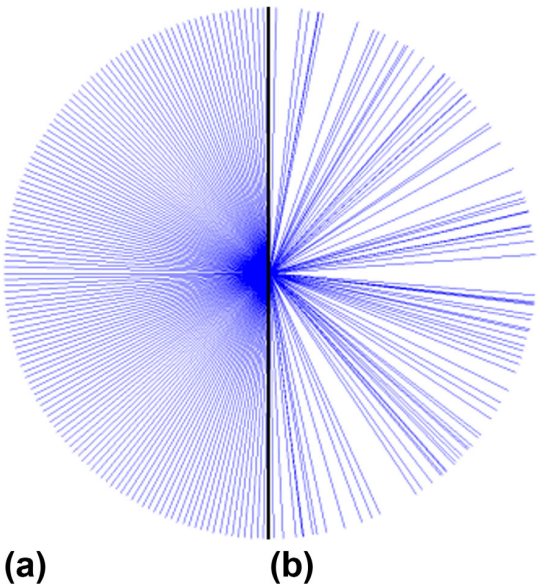

FIG. 2. K-space profile distribution in TPM_{Ref} (left half, **a**), and TPM_{SG} (right half, **b**). K-space is sampled with $R = 2$ (132 profiles) with equally spaced profiles in the prospective acquisition, and randomly undersampled (here: 90 profiles) with good k-space coverage in the retrospective scan.

$\Delta r = \int_0^T \frac{\int v(r,t)\mu(r,t)dr}{\int \mu(r,t)dr} dt$ with T being the length of the cardiac cycle. Residual displacement should be close to zero, considering the physiological constraint that each voxel of the myocardium should return to its initial position after completion of a full cardiac cycle.

All quality measures were statistically compared by a Wilcoxon signed-rank test and *P*-values below 5% were considered significant.

RESULTS

Acquisition

The acquisitions could be performed successfully in all cases. Mean navigator efficiency of the TPM_{ref} scans resulted as $61 \pm 10\%$, yielding an average scan duration of 4 min 48 s $\pm$ 18 s per slice. Self-gating was successful in all TPM_{SG} scans and coverage of the complete cardiac cycle could be obtained.

Figure 2 shows the distribution of the radial k-space profiles in TPM_{Ref} and TPM_{SG}. Profiles are equally spaced and fulfill the radial Nyquist theorem in the prospective acquisition (Fig. 2a), whereas the k-space is randomly undersampled due to the retrospective ECG synchronization with good coverage of the k-space (average angle between radial profiles $= 3.7^\circ \pm 4^\circ$) due to the golden angle acquisition scheme in the self-gated scan (Fig. 2b).

Self-Gating

Figure 3 shows a representative example of the image quality of the sliding-window data applied for retrospective generation of the self-gating (SG) signal in a

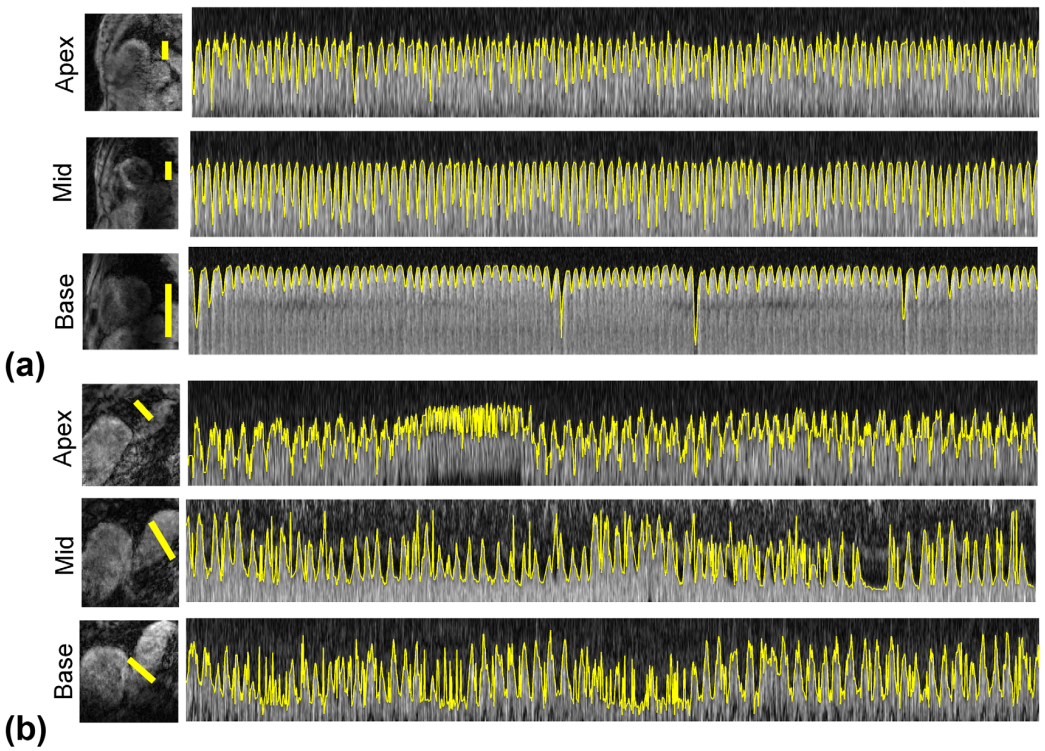

FIG. 3. Placement of the SG profile in the sliding window images and the resulting image-based SG signals from the acquired short axis views in a volunteer (**a**) and the patient (**b**).

volunteer (Fig. 3a) and in the patient (Fig. 3b). A sufficient gating signal could be generated from the liver-lung interface for apical, mid-ventricular, and basal views from all TPM_{SG} data. After gating with the window of 8 mm, and only taking the first 4 min 48 s of the acquisition into account to match the acquisition time of TPM_{Ref}, an average undersampling factor of $R = 3.0 \pm 0.9$ (98 ± 27 radial profiles) resulted for the TPM_{SG} scans.

Image Quality

Magnitude and velocity images of TPM_{Ref} and TPM_{SG} in systole and diastole are shown in Figure 4, and respective CINE movies are available in the Supporting Videos, which are available online. Quantitative comparison of all investigated image quality and velocity measures is summarized in Table 2.

Visually, magnitude images from both acquisitions show similar sharpness and noise level and slightly superior contrast of TPM_{SG} in diastole (Fig. 4). CV_M^{-1} of TPM_{SG} is significantly reduced for $\lambda = 0.1$ and significantly increased for $\lambda \in \{0.3, 0.4\}$, but similar to TPM_{Ref} for $\lambda = 0.2$ (as shown in Figure 4). While image sharpness is comparable for all reconstructions, contrast is significantly improved in TPM_{SG} for all λ. While slight streaking artifacts can be observed for TPM_{SG} in the CINE movies, expert image score (difficulty of segmentation) reveals similar values for different reconstructions, with higher scores increasing from the apical to the basal slice.

Velocity Analysis

The noise level in the velocity images is visually comparable (Fig. 4). Also, CV_V^{-1} values do not differ significantly from the values of TPM_{Ref} (Table 1).

Plots of the regional velocities obtained in 24 segments as well as the global velocities are shown exemplarily for one volunteer in Figure 5. As suggested in Simpson et al (9), the velocities are plotted in a color scale for the myocardial segments over the cardiac cycle. Where in TPM_{SG} full coverage of the cardiac cycle is obtained, in TPM_{ref} the first 35 ms and the last 5% of the cardiac cycle are not covered due to the trigger delay of the ECG synchronization, RNAV measurements, and a safety margin required for considering changes in the heart beat frequency. Thus, no A wave velocities could be derived from TPM_{Ref} data, whereas they are covered by TPM_{SG}. Otherwise, the v-t curves appear visually similar for the investigated acquisition and reconstruction techniques. A slight reduction in the peak velocities may be observed for TPM_{SG} data, especially in case of strong regularization.

Timings of longitudinal and radial S and E waves are similar in TPM_{Ref} and TPM_{SG} for all investigated λ (except the longitudinal E wave for $\lambda = 0.4$). However, a tendency toward reduced amplitudes with increase of λ can be observed, which reaches significance for strong regularization (except the radial E wave, where the reduction is also significant for less strong regularization). This peak reduction depends linearly on λ for the investigated range (Pearson correlation coefficients $|r| = 0.99 \pm 0.03$; $P < 5\%$ in 173 of 180 cases).

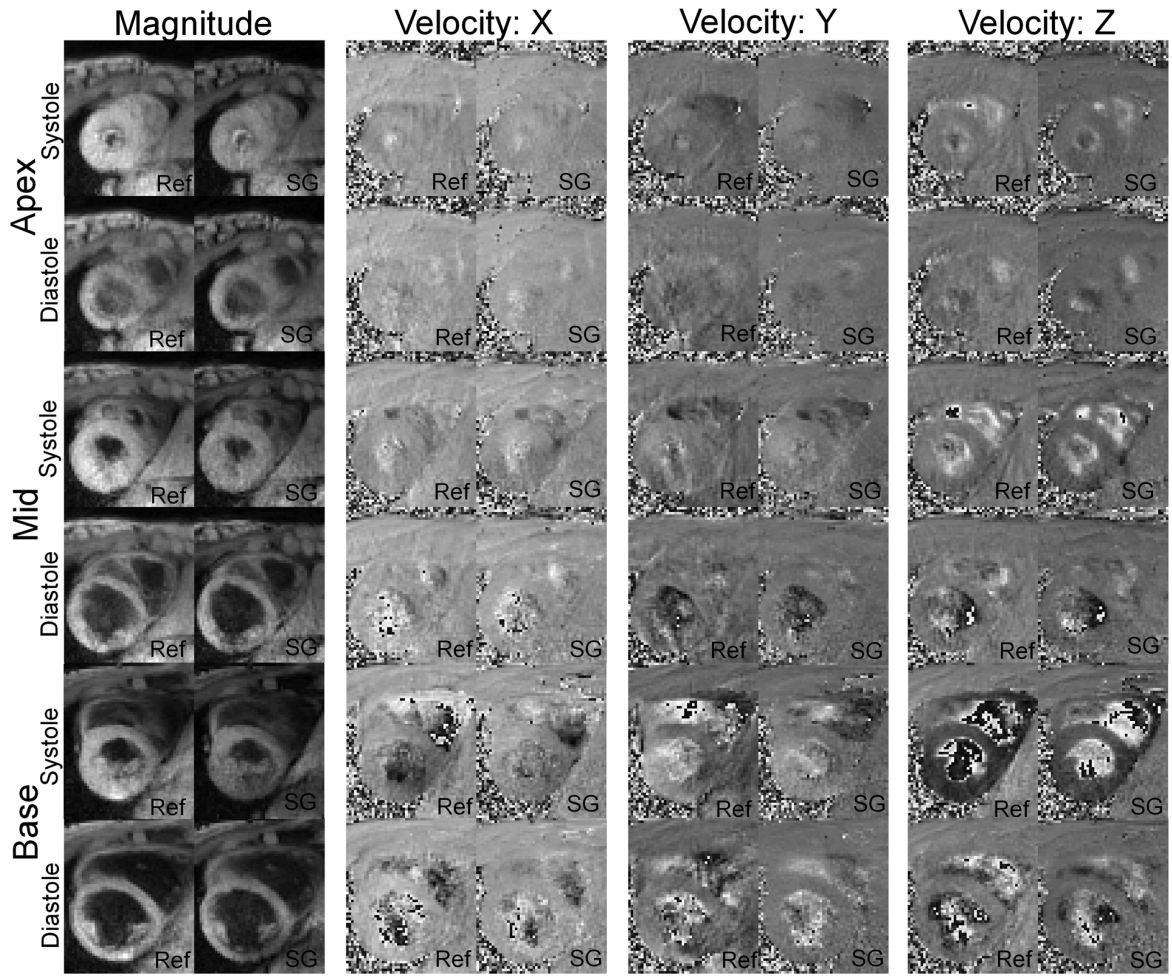

FIG. 4. Comparison of magnitude and velocity image quality between TPM_{Ref} (left) and TPM_{SG} with $\lambda = 0.2$ (right) for all slices in systole and diastole in a volunteer. Cine movies to this figure are available in the Supporting Videos.

Quantitative analysis of the segmental v-t curves confirms the visual impression of similar motion patterns by average correlation values above 0.8 and average RMSE values below 0.11 cm/s in all cases.

Residual displacements Δr were significantly reduced in TPM_{SG} for all investigated λ compared with TPM_{Ref}. Generally, higher values of longitudinal Δr were observed due to the higher velocities in this direction.

Magnitude and velocity images of TPM_{SG} in the patient are shown in Figure 6. While blood suppression is reduced due to impaired contraction of the heart, sufficient delineation of endocardial an epicardial borders can be appreciated in the velocity images, which supports the segmentation of the myocardium.

Segmental velocities of the patient in all three slices are shown in Figure 7. Peak velocities are reduced compared with the healthy volunteers. Velocity patterns exhibit features of impaired motion also visible in two-chamber, four-chamber, and short axis views (see Supporting Videos). For example, earlier contraction of the lateral wall and later contraction of the septal wall can be appreciated from the radial velocities, and opposite movement of lateral and septal wall at the A peak time can be observed from the longitudinal velocities, especially in the apical slice.

DISCUSSION

In this study, retrospectively triggered self-gated radial golden angle TPM (TPM_{SG}) was evaluated against a conventional prospective, navigator-gated TPM acquisition (TPM_{ref}) in healthy volunteers. The combination of the continuous self-gating approach based on the golden angle acquisition geometry and compressed sensing reconstruction techniques enabled the acquisition of high-quality TPM images in acquisition times comparable to the conventional TPM_{ref} approach.

Self-Gating

In this contribution, image-based self-gating was applied. It was shown earlier (17) that the image-based approach performs more reliable than profile-based approaches. This may especially be the case in combination with golden angle acquisition techniques, in which rapidly changing eddy currents caused by the required huge

Table 2
Comparison of TPM_{Ref} and TPM_{SG} for Different Regularization Strengths by Means of Image Quality Measures and Velocity Peaks, Peak Times, Correlation, RMSE, and Residual Displacement[a]

			TPM_{SG}			
Measure		TPM_{Ref}	$\lambda = 0.1$	$\lambda = 0.2$	$\lambda = 0.3$	$\lambda = 0.4$
CV_M^{-1}		6.5±1.2	6.0±1.1*	6.6±1.4	7.0±1.6*	7.3±1.8*
Sharpness		0.116±0.061	0.120±0.062	0.124±0.064	0.126±0.066	0.127±0.066
Contrast		0.18±0.07	0.21±0.08*	0.22±0.08*	0.22±0.09*	0.22±0.09*
Score	apex	2.1±0.3	2.6±0.7	2.5±0.5	2.5±0.7	2.6±0.7
	mid	3.0±0.8	3.5±0.7	3.6±0.8	3.8±0.9	3.8±0.9
	base	3.7±0.8	3.5±0.7	3.8±0.6	4.0±0.7	4.0±0.7
CV_V^{-1}	X	2.5±0.77	2.3±0.62	2.4±0.67	2.5±0.71	2.5±0.72
	Y	2.7±0.58	2.5±0.54	2.6±0.55	2.6±0.56	2.6±0.55
	Z	3.4±0.99	3.1±0.83	3.2±0.86	3.2±0.88	3.2±0.90
Radial peaks (cm/s)	S	3.1±0.3	3.1±0.4	3.0±0.4	2.9±0.4	2.8±0.4*
	E	−5.2±0.8	−4.5±0.8*	−4.3±0.8*	−4.1±0.8*	−3.9±0.8*
	A	N/A	−1.7±0.6	−1.5±0.5	−1.3±0.5	−1.2±0.4
Longitudinal peaks (cm/s)	S	6.2±2.4	5.9±2.0	5.5±2.1	5.2±2.1*	4.9±2.1*
	E	−7.9±3.1	−7.2±3.0	−6.9±3.0	−6.5±2.9	−6.2±2.9*
	A	N/A	−3.2±1.0	−2.9±1.0	−2.6±0.9	−2.3±0.9
Radial peak times (ms)	S	131±29	135±35	135±33	138±35	144±36
	E	471±36	469±38	469±38	469±37	469±37
	A	N/A	858±166	857±164	857±163	857±163
Longitudinal peak times (ms)	S	70±12	72±15	72±15	74±15	75±15
	E	456±62	450±61	450±57	449±58	447±56*
	A	N/A	859±167	859±165	859±165	859±165
Velocity correlation	rad.		0.88±0.08	0.89±0.08	0.89±0.08	0.89±0.08
	circ.		0.80±0.13	0.81±0.13	0.81±0.13	0.80±0.13
	long.		0.90±0.10	0.90±0.10	0.90±0.10	0.90±0.11
Velocity RMSE (cm/s)	rad.		0.09±0.03	0.09±0.03	0.09±0.0	0.09±0.03
	circ.		0.08±0.03	0.08±0.03	0.08±0.03	0.08±0.03
	long.		0.11±0.04	0.10±0.04	0.11±0.04	0.11±0.04
Δr (mm)	rad.	9.9±8.1	6.4±5.2*	6.3±5.1*	6.3±5.1*	6.3±5.1*
	circ.	11.3±9.5	6.6±5.5*	6.6±5.4*	6.5±5.3*	6.5±5.3*
	long.	12.9±9.2	8.4±7.1*	8.7±7.1*	8.7±7.1*	8.9±7.2*

[a]Values are presented as "mean ± standard deviation," and statistically significant differences compared to TPM_{Ref} are marked by an asterisk.

angular gaps between subsequent projections likely impact the quality of the gating signal retrieved from single projections or k-space points. Even though the acquisition window for the required sliding window reconstruction had to be prolonged due to the interwoven flow encoding, excellent quality of the gating signal could be achieved in all volunteers.

Image Quality

Using a golden angle trajectory had three synergetic effects on image quality, (i) the reconstruction window for the image-based navigator could be chosen freely for sufficient temporal resolution of the self-gating signal, (ii) the uniform distribution property of the golden angle ordering for arbitrary sub-windows (16) leads to a near-uniform distribution in the set of accepted profiles, in contrast to a conventional radial trajectory that propagates the formation of blocks and gaps, and (iii) the k-space profiles accepted by the gating still exhibit a temporal incoherence that is a prerequisite for the compressed sensing reconstruction.

CV_M^{-1} and CV_V^{-1} from TPM_{SG} with regularization strength set to $\lambda = 0.2$ were comparable to those of TPM_{Ref}. Higher values of λ led to reduced velocity variability (increased CV_V^{-1}) due to the smoothing effect of the temporal regularization, while weaker regularization ($\lambda = 0.1$) resulted in higher noise levels and streaking artifacts and thus decreased CV_M^{-1}. While reliable SNR and VNR measurements from compressed sensing reconstructions cannot be obtained easily due to the nonlinearity of the reconstruction method, the inverse of the magnitude and velocity variability allow a quantitative investigation of smoothing effects of the reconstruction. Reduced values of CV_M^{-1} were found because strong regularization leads to image smoothing, but values for $\lambda = 0.2$ were comparable to the CV_M^{-1} and CV_V^{-1} measurements of TPM_{Ref} reconstructed by gridding, i.e., without any smoothing in the reconstruction. Image sharpness and myocardium-to-blood contrast were almost independent of the regularization strength. While sharpness was similar to TPM_{Ref}, contrast was significantly improved in TPM_{SG}. This was to be expected, because the width of the blood saturation bands had to be reduced for TPM_{Ref} to avoid interference with the RNAV measurement, leading to reduced black-blood contrast during phases of rapid blood flow, while the saturation bands could be applied at full width in TPM_{SG}.

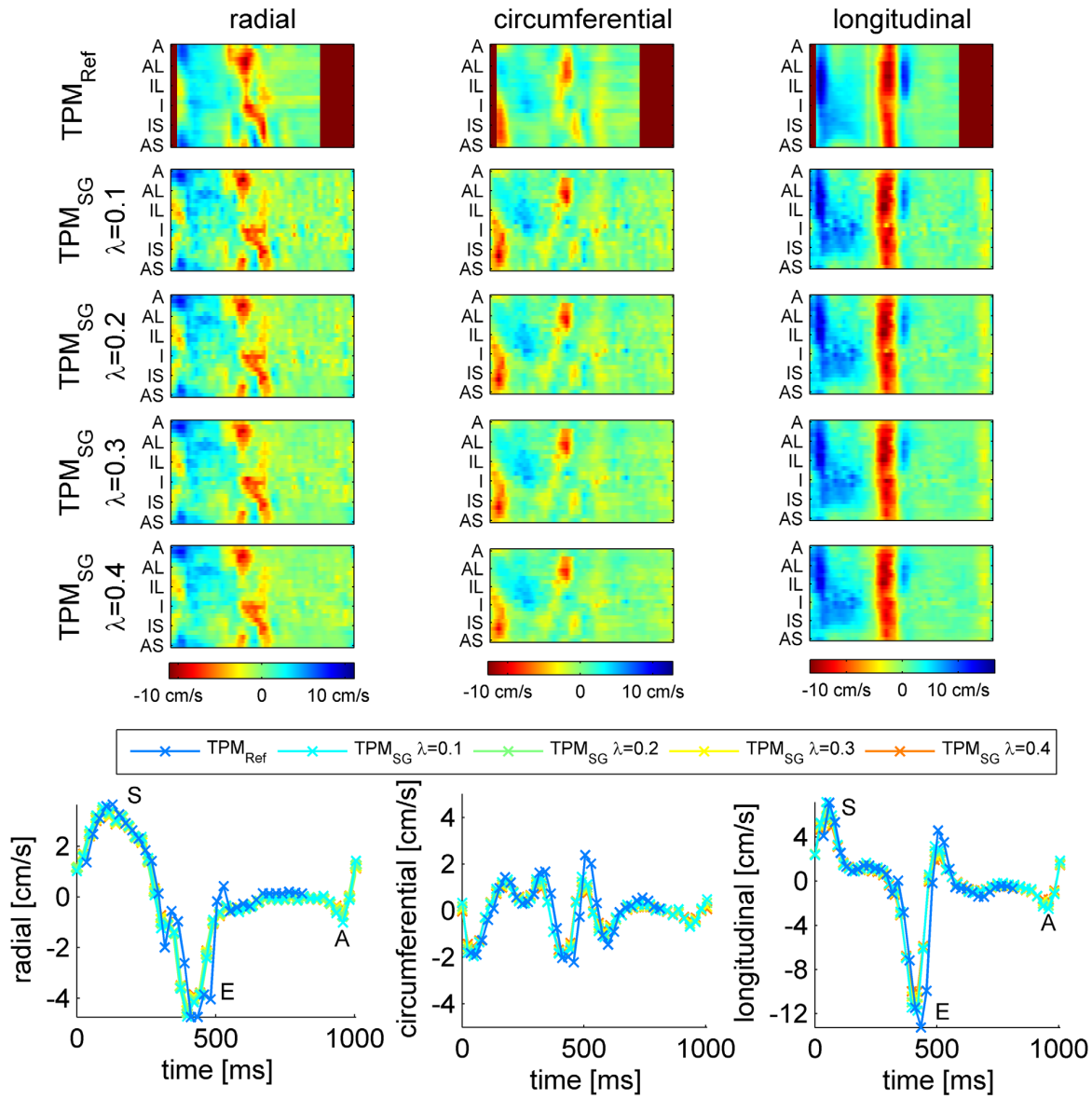

FIG. 5. Plots of the segmental (top) and global (bottom) velocities over the cardiac cycle for visualization of the motion patterns in the different velocity directions in one volunteer for the different acquisitions and reconstructions. Abbreviations of the segments: A, anterior; AL, anterolateral; IL, inferolateral; I, inferior; IS, inferoseptal; AS, anteroseptal.

Image quality scores for this study were defined by means of the difficulty of segmentation, i.e., the delineation of endocardium and epicardium. This is mainly influence by blood-myocardium contrast, sharpness of the myocardial edges, and presence or absence of image artifacts. Although slightly more streaking artifacts were visible in TPM_{SG} than in TPM_{Ref} due to the increased undersampling, scores were comparable between TPM_{Ref} and TPM_{SG}, and showed a slight tendency toward increased score with increase of λ, which can be attributed to the reduction of streaks with stronger regularization. Generally, image scores for basal slices were higher than those for mid-level slices, and mid-level scores were higher than apical scores. This is due to the decreasing size of the blood pool from base to apex, which makes the delineation of the endocardium more difficult, especially during systole.

Velocity Analysis

Velocity-to-noise ratios were similar between TPM_{Ref} and TPM_{SG}. While peak timings of radial and longitudinal S and E waves ware comparable for all reconstructions, the peak amplitudes showed a tendency toward reduces values with increasing regularization. This tendency was found to be almost linear for the investigated range. The decrease of peak amplitudes is due to the temporal regularization, which results in a smoothing

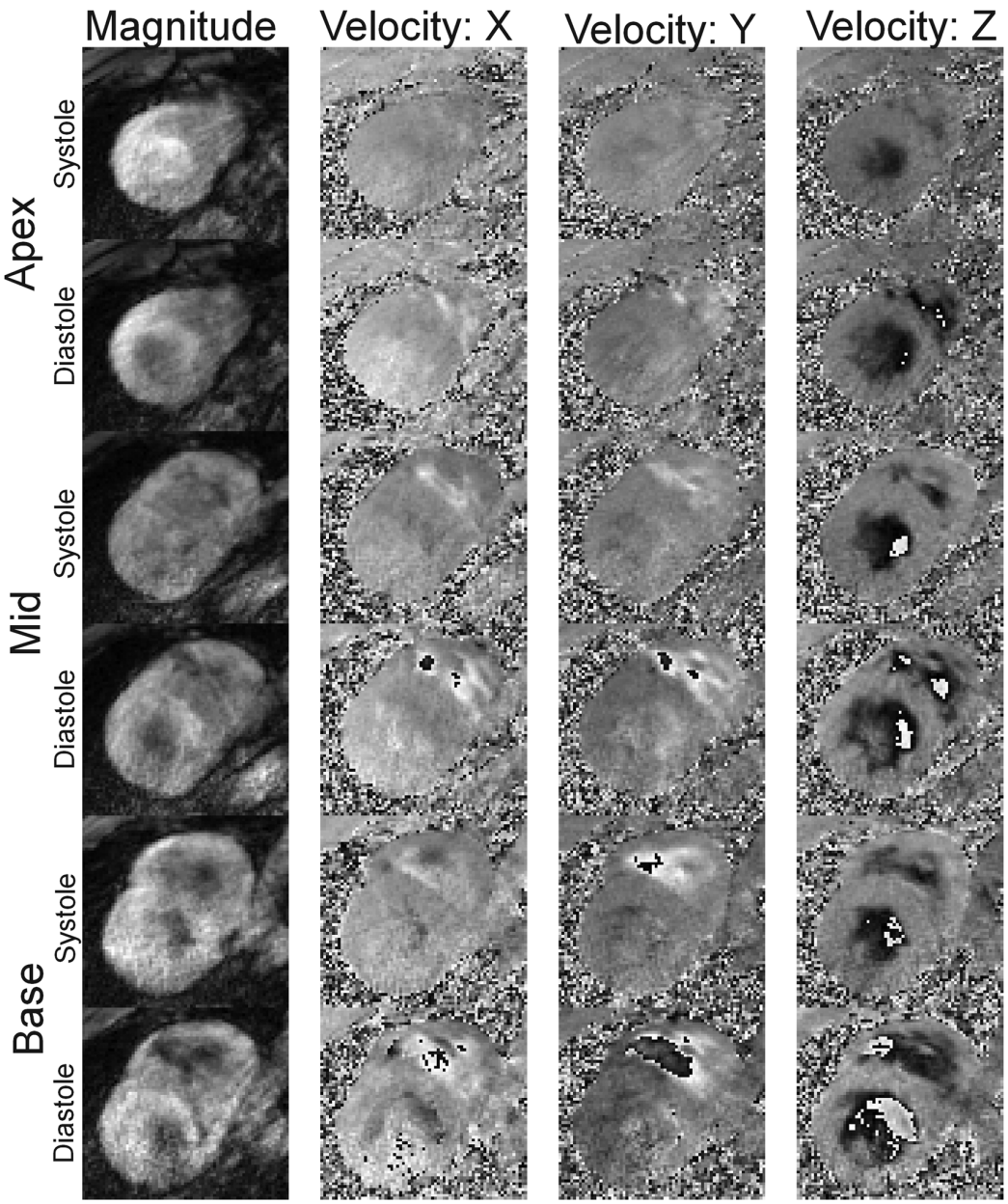

FIG. 6. Magnitude and velocity images for TPM_{SG} with $\lambda = 0.2$ for all slices in systole and diastole in the patient. Acquisitions with TPM_{Ref} were not performed due to scan time restrictions.

effect along the time dimension. Similar reduction in the peak velocities have also be reported earlier for SENSE (12) or kt-BLAST (11) in combination with high undersampling factors. No significant differences in peak velocities were found in spiral TPM (13) for low undersampling factors of $R = 2$ and $R = 2.67$, which is in line with the findings of this study, because low undersampling requires little regularization, especially for trajectories where the k-space center is still almost fully covered.

Segmental velocities were investigated for 24 segment as required as input information for quantitative analysis (3). The visual impression of comparable motion patterns in TPM_{Ref} and TPM_{SG} was confirmed by correlation values in the order of 0.8–0.9 and low RMSE < 0.11 cm/s. Reduced correlation values may be attributed to interpolation necessary to evaluate velocities from TPM_{Ref} and TPM_{SG} at the same times of the cardiac cycle although measured at slightly different time points. Analysis of the residual displacement after integration of the mean velocities over the entire cardiac cycle revealed a significant lower error in case of TPM_{SG}. This can likely be attributed to the more complete coverage of the entire cycle with the self-gated technique and the availability of a continuous gating signal. Complete disappearance of the error cannot be expected due to through-plane motion and the limited temporal resolution of the analysis.

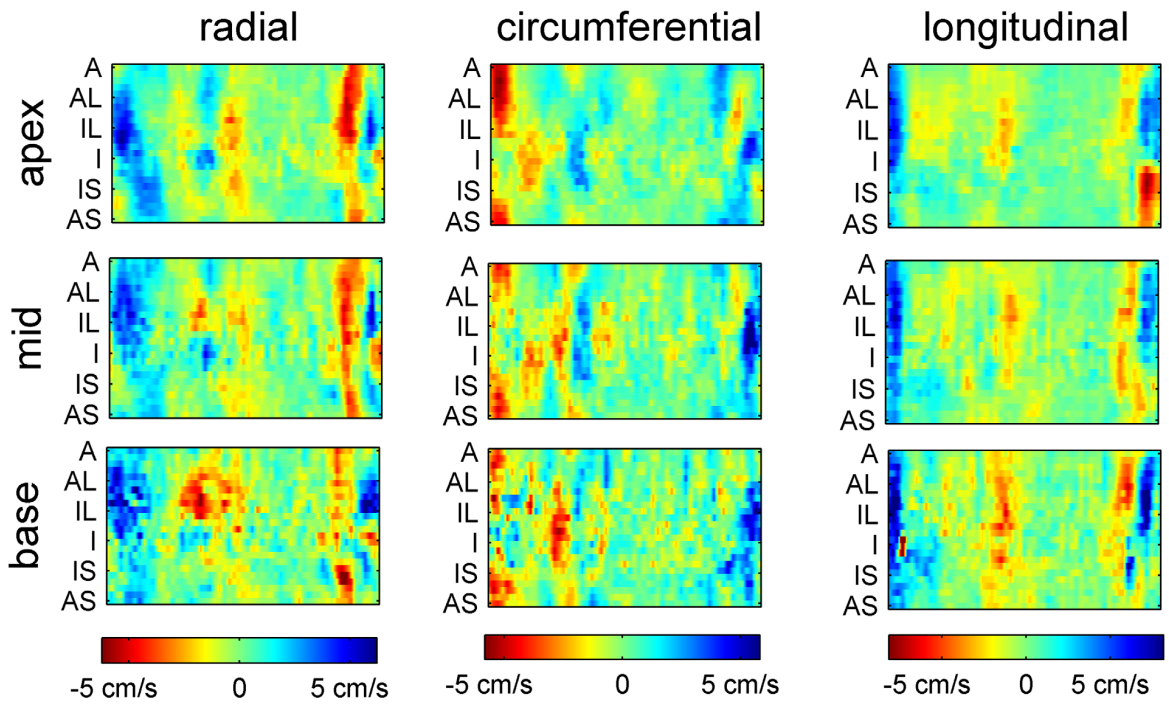

FIG. 7. Segmental velocities of the patient from TPM_{SG} in all slices reconstructed with $\lambda = 0.2$. Long axis and short axis planning scans from the mid-level slice are available as Supporting Videos.

Limitations

In its current form, the proposed approach still demands rather long acquisition times, which might limit the widespread clinical use of the technique. Simpson et al (13) showed the feasibility of using breathhold acquisitions by combining TPM with spiral data acquisition. However, the required high number of cardiac cycles may limit the application of the technique in patients with severe myocardial impairment and does not easily allow further increasing spatial resolution. The unique properties of radial MRI appear advantageous in case of residual motion or close to metal objects like stents or after open chest surgery. Which of the approaches will finally turn out to be of clinical value needs to be evaluated.

Two separate free-breathing acquisitions (approximately 20 s each) per slice were performed for calculation of the coil sensitivity maps. To further reduce scan time and simplify the scanning procedure, the averaged data from the TPM acquisition itself could be used for calculation of the coil sensitivities, thus eliminating one of the coil calibration scans.

The indication of the line used for the evaluation of the self-gating signal requires user interaction before reconstruction of the high-fidelity TPM data and makes the technique not fully automatic. However, integration of the SG technique into an interactive graphical user interface allows immediate inspection of the quality of the resulting SG signal and enables direct improvement by interactive modification of the profile position, which might be advantageous compared with fully automated approaches, such as SG from image correlation (15), because it facilitates using the direct displacement of the target organ for gating instead of applying indirect measures. Furthermore, e.g., in case the liver is not visible in the imaging slice other features such as the lung/heart interface can be selected to yield a good SG signal even in complicated anatomic situations. However, the robustness of the proposed method needs to be further evaluated in a larger patient group with different cardiac pathologies.

Reconstructions were performed on an Intel Xeon E5 1.8 GHz CPU (4 Cores) and with 128 GB RAM available, and gridding and regridding were performed on a NVIDIA Tesla K20c GPU (with 5 GB memory). Currently, clinical usability is still constricted by the rather long iterative reconstruction times of 2 h (sliding window reconstruction) and 30 min (TPM_{SG}). This can be improved by implementation of the complete reconstruction process on the GPU, including calculation of coil sensitivity maps, thus taking advantage of the highly parallel execution compared with the CPU. Reduction of the amount of data to be processed could also shorten reconstruction times and enable processing of all data on the limited GPU memory at once. Data reduction could be achieved by coil array compression (37), although its influence on velocity data remains to be investigated.

Summary

Considering the good correlation and low RMSE of the v-t curves obtained from the TPM_{SG} scans compared with the conventional TPM_{ref} technique, the only slight bias in the peak velocities and the improved

performance of TPM_{SG} for the residual displacement, TPM_{SG} appears a promising candidate for providing quantitative velocity data as basis for further evaluation of motion impairment parameters. By choice of the regularization strength $\lambda = 0.2$, the effect of reduced peaks is still small, while comparable image quality and sharpness, and superior contrast can be achieved. The intrinsic robustness of radial acquisition techniques regarding residual motion, the applicability of the golden angle data for compressed sensing techniques, and the possibility of retrieving continuous high-quality self-gating information from the imaging data without any compromises in imaging speed underlines the potential of the suggested TPM_{SG} technique.

CONCLUSIONS

We successfully applied Golden Angle Radial Sparse SENSE in combination with image-based self-gating for high-quality high-resolution velocity encoded MRI of the myocardium. It was shown that the temporal TV regularization applied for reconstruction provided excellent fidelity velocity information when compared with the conventional navigated approach. Superior black-blood contrast resulted into excellent conspicuity of the endocardium. The reconstructed motion information may facilitate further quantification of motion impairment parameters.

ACKNOWLEDGMENTS

V.R. and J.P. were funded by a research grant from Philips Healthcare and by the NVIDIA Hardware Donation Program (GPU donations).

REFERENCES

1. Bijnens B, Claus P, Weidemann F, Strotmann J, Sutherland GR. Investigating cardiac function using motion and deformation analysis in the setting of coronary artery disease. Circulation 2007;116:2453–2464.
2. Cheung Y. The role of 3D wall motion tracking in heart failure. Nat Rev Cardiol 2012;9:644–657.
3. Lutz A, Paul J, Bornstedt A, Nienhaus GU, Etyngier P, Bernhardt P, Rottbauer W, Rasche V. Volumetric motion quantification by 3D tissue phase mapped CMR. J Cardiovasc Magn Reson 2012;14:1–13.
4. Axel L, Dougherty L. MR imaging of motion with spatial modulation of magnetization. Radiology 1989;171:841–845.
5. Aletras A, Ding S, Balaban R, Wen H. DENSE: displacement encoding with stimulated echoes in cardiac functional MRI. J Magn Reson 1999;137:247–252.
6. Osman NF, Sampath S, Atalar E, Prince JL. Imaging longitudinal cardiac strain on short-axis images using strain-encoded MRI. Magn Reson Med 2001;46:324–334.
7. Maret E, Todt T, Brudin L, Nylander E, Swahn E, Ohlsson JL, Engvall JE. Functional measurements based on feature tracking of cine magnetic resonance images identify left ventricular segments with myocardial scar. Cardiovasc Ultrasound 2009;7:53.
8. Bryant DJ, Payne A, Firmin DN, Longmore DB. Measurement of flow with NMR imaging using a gradient pulse and phase difference technique. J Comput Assist Tomogr 1984;8:588–593.
9. Simpson R, Keegan J, Firmin D. Efficient and reproducible high resolution spiral myocardial phase velocity mapping of the entire cardiac cycle. J Cardiovasc Magn Reson 2013;15:34.
10. Simpson RM, Keegan J, Firmin DN. MR assessment of regional myocardial mechanics. J Magn Reson Imaging 2013;37:576–599.
11. Lutz A, Bornstedt A, Manzke R, Etyngier P, Nienhaus GU, Rasche V. Acceleration of tissue phase mapping by kt BLAST: a detailed analysis of the influence of kt-BLAST for the quantification of myocardial motion at 3T. J Cardiovasc Magn Reson 2011;13:5.
12. Lutz A, Borstedt A, Etyngier P, Nienhaus GU, Rottbauer W, Rasche V. Acceleration of tissue phase mapping with sensitivity encoding at 3T. J Cardiovasc Magn Reson 2011;13:5.
13. Simpson R, Keegan J, Gatehouse P, Hansen M, Firmin D. Spiral tissue phase velocity mapping in a breath-hold with non-cartesian SENSE. Magn Reson Med 2014;72:659–668.
14. Kellman P, Chefd'hotel C, Lorenz CH, Mancini C, Arai AE, McVeigh ER. Fully automatic, retrospective enhancement of real-time acquired cardiac cine MR images using image-based navigators and respiratory motion-corrected averaging. Magn Reson Med 2008;59:771–778.
15. Steeden JA, Knight DS, Bali S, Atkinson D, Taylor AM, Muthurangu V. Self-navigated tissue phase mapping using a golden-angle spiral acquisition—proof of concept in patients with pulmonary hypertension. Magn Reson Med 2014;71:145–155.
16. Winkelmann S, Schaeffter T, Koehler T, Eggers H, Doessel O. An optimal radial profile order based on the golden ratio for time-resolved MRI. IEEE Trans Med Imaging 2007;26:68–76.
17. Paul J, Divkovic E, Wundrak S, Bernhardt P, Rottbauer W, Neumann H, Rasche V. High-resolution respiratory self-gated golden angle cardiac MRI: comparison of self-gating methods in combination with k-t SPARSE SENSE. Magn Reson Med 2014. doi: 10.1002/mrm.25102.
18. Candes E, Romberg J, Tao T. Robust uncertainty principles: exact signal reconstruction from highly incomplete frequency information. IEEE Trans Inf Theory 2005;52:489–509.
19. Lustig M, Donoho DL, Santos JM, Pauly JM. Compressed sensing MRI. IEEE Signal Process Mag 2008;25:72–82.
20. Gamper U, Boesiger P, Kozerke S. Compressed sensing in dynamic MRI. Magn Reson Med 2008;59:365–373.
21. Otazo R, Kim D, Axel L, Sodickson DK. Combination of compressed sensing and parallel imaging for highly accelerated first-pass cardiac perfusion MRI. 2010;64:767–776.
22. Adluru G, McGann C, Speier P, Kholmovski EG, Shaaban A, DiBella EVR. Acquisition and reconstruction of undersampled radial data for myocardial perfusion magnetic resonance imaging. J Magn Reson Imaging 2009;29:466–473.
23. Feng L, Grimm R, Block KT, Chandarana H, Kim S, Xu J, Axel L, Sodickson DK, Otazo R. Golden-angle radial sparse parallel MRI: combination of compressed sensing, parallel imaging, and golden-angle radial sampling for fast and flexible dynamic volumetric MRI. Magn Reson Med 2014;72:707–717.
24. Lutz A, Bornstedt A, Manzke R, Nienhaus GU, Etyngier P, Rasche V. SAR reduced black-blood cine TPM for increased temporal resolution at 3T. Magn Reson Mater Phys Biol Med 2011;24:127–135.
25. Keeling SL, Bammer R. A variational approach to magnetic resonance coil sensitivity estimation. Appl Math Comput 2004;158:359–388.
26. Allison MJ, Ramani S, Fessler JA. Regularized MR coil sensitivity estimation using augmented lagrangian methods. In 9th International Symposium on Biomedical Imaging (ISBI), Barcelona, Spain, 2012. pp. 394–397.
27. Otsu N. A threshold selection method from gray-level histograms. IEEE Trans Syst Man Cybern 1979;9:62–66.
28. Freedman D, Diaconis P. On the histogram as a density estimator: L 2 theory. Probab Theory Relat Fields 1981;57:453–476.
29. Wundrak S, Paul J, Ulrici J, Hell E, Kozerke S, Rasche V. Sparse dynamic MRI with an adaptive temporal sparsity prior for cardiovascular imaging. In Proceedings of the 22nd Annual Meeting of ISMRM, Milano, Italy, 2014. Abstract 4384.
30. Rasche V, Proksa R, Sinkus R, Bornert P, Eggers H. Resampling of data between arbitrary grids using convolution interpolation. IEEE Trans Med Imaging 1999;18:385–392.
31. Hager WW, Zhang H. A new conjugate gradient method with guaranteed descent and an efficient line search. SIAM J Optim 2005;16:170–192.
32. Nocedal J, Wright SJ. Numerical optimization. Second edition. New York: Springer; 2006.
33. Walker PG, Cranney GB, Scheidegger MB, Waseleski G, Pohost GM, Yoganathan AP. Semiautomated method for noise reduction and background phase error correction in MR phase velocity data. J Magn Reson Imaging 1993;3:521–530.

34. Hautvast G, Lobregt S, Breeuwer M, Gerritsen F. Automatic contour propagation in cine cardiac magnetic resonance images. IEEE Trans Med Imaging 2006;25:1472–1482.
35. Fradkin M, Ciofolo C, Mory B, Hautvast G, Breeuwer M. Comprehensive segmentation of cine cardiac MR images. Med Image Comput Comput Assist Interv 2008;2008:178–185.
36. Larson AC, Kellman P, Arai A, Hirsch GA, McVeigh E, Li D, Simonetti OP. Preliminary investigation of respiratory self-gating for free-breathing segmented cine MRI. Magn Reson Med 2005;53:159–168.
37. Buehrer M, Pruessmann KP, Boesiger P, Kozerke S. Array compression for MRI with large coil arrays. Magn Reson Med 2007;57:1131–1139.
38. Pelc NJ, Bernstein MA, Shimakawa A, Glover GH. Encoding strategies for three-direction phase-contrast MR imaging of flow. J Magn Reson Imaging 1991;1:405–413.

SUPPORTING INFORMATION

Additional Supporting Information may be found in the online version of this article.

Supporting Video TPM_Ref.avi: Cine magnitude and velocity images from TPM_{Ref} from one volunteer in a mid-ventricular slice.
Supporting Video TPM_SG.avi: Cine magnitude and velocity images from TPM_{SG} reconstructed with $\lambda = 0.2$ from one volunteer in a mid-level slice.
Supporting Video patient_4CH.avi: Four-chamber view cine planning scan of the patient.
Supporting Video patient_2CH.avi: Two-chamber view cine planning scan of the patient.
Supporting Video patient_SA.avi: Mid-ventricular short axis cine planning scan of the patient.

6 Cardiac Self-Gating and Non-Uniform Self-Gating

This article [18] was published as

Wundrak, S., Paul, J.*, Ulrici, J., Hell, E., Geibel, M.-A., Bernhardt, P., Rottbauer, W., and Rasche, V. (2015), A Self-Gating Method for Time-Resolved Imaging of Non-Uniform Motion. Magn Reson Med. doi: 10.1002/mrm.26000.*

and is © 2015 by Wiley Periodicals, Inc. Reprinted with permission.

** = contributed equally (see acknowledgments at the end of the article)*

NOTE

Magnetic Resonance in Medicine 00:00–00 (2015)

A Self-Gating Method for Time-Resolved Imaging of Nonuniform Motion

Stefan Wundrak,[1,2]* Jan Paul,[1] Johannes Ulrici,[2] Erich Hell,[2] Margrit-Ann Geibel,[3] Peter Bernhardt,[1] Wolfgang Rottbauer,[1] and Volker Rasche[1]

Purpose: To develop a self-gating method capable of assessing nonuniform motion, e.g., in cardiovascular magnetic resonance imaging of patients with severe arrhythmia, or for imaging of the temporomandibular joint.
Methods: The proposed method allows cyclic motion trajectories with a nonuniform pace by replacing the one-dimensional gating signal of conventional image-based self-gating with a two-dimensional gating matrix. The resulting image quality is compared with conventional self-gating and real-time MRI.
Results: Nonuniform self-gating resulted in superior image quality compared with conventional self-gating and the feasibility study showed significantly improved image sharpness ($P < 0.01$). Further, improvements in image quality were shown compared with golden angle radial parallel sparse MRI.
Conclusion: A new self-gating method was proposed that allows cardiovascular magnetic resonance of arrhythmic patients, which is a common problem in clinical practice. Further, the proposed method enables self-gated imaging of the temporomandibular joint. **Magn Reson Med 000:000–000, 2015. © 2015 Wiley Periodicals, Inc.**

Key words: self-gating; cine; cardiac; cardiovascular magnetic resonance; temporomandibular joint; arrhythmia

INTRODUCTION

Prospective electrocardiogram (ECG) triggered acquisition has become the de facto standard for cardiovascular magnetic resonance imaging. Despite the use of rapid, accelerated real-time cine imaging (1,2), ECG gated (3) or retrospective self-gated techniques for cine imaging (4–6) achieve better image quality in terms of signal-to-noise ratio (SNR) for a comparable temporal and spatial resolution provided that no additional artifacts occur due to wrong binning caused by irregular heart beats or patient movement.

Gating methods usually identify a reference (zero-phase) position (e.g., R wave) for each cycle. Under the assumption that all cycles show identical motion, a fully sampled k-space dataset is compiled from k-space data acquired during multiple motion cycles.

In case of e.g., cardiac arrhythmia the assumption of identical motion cycles is not valid, as the contraction of the myocardium is a complex, nonlinear movement, and cardiac motion phases show a highly nonlinear relation to the heart rate (7,8). Therefore, simple linear rescaling of the cardiac motion phases to the ECG signal will lead to wrong binning and artifacts or temporal blurring. In current practice, cycles deviating substantially from the mean interval are discarded. This leads to increased acquisition time and often degraded image quality. Furthermore, information about the arrhythmic motion is lost.

While real-time imaging was successfully used for cardiovascular imaging, in particular in case of arrhythmia, the clinical evaluation is still ongoing. More specifically, all real-time methods that achieve the necessary temporal resolution of 20–50 ms use temporal regularization or filtering and the impact on the effective temporal resolution/functional parameters is still under debate. For example, Voit et al. (1) reported a 10% lower ejection fraction for real-time imaging compared with breath-hold ECG gated imaging, which was confirmed by our preliminary results (9). In contrast, Aandal et al. (2) did not report any deviations in global functional parameters. A gating method capable of imaging arrhythmia might circumvent these challenges and will fit well into the existing clinical routine of gated acquisitions.

Similar to cardiac arrhythmia, self-gated imaging of active joint motion is prevented by the usually not perfectly reproducible motion cycles, e.g., for imaging of the moving temporomandibular joint (TMJ) (10,11).

In this work, we propose a self-gating method that uses a two-dimensional gating matrix without presuming identical motion cycles, but motion cycles that at least partially follow the same motion trajectory, possibly at a different pace.

METHODS

Image-Based Self-Gating

Larson et al. (5) suggested to reconstruct a preliminary image series m with low spatial and high temporal resolution using a sliding window reconstruction with window width w. The image series m is restricted to a region of interest containing the myocardial wall. The one-dimensional self-gating signal g is defined using the Pearson correlation ρ (12) of all images m_n to a selected template image m_t

$$g_n = \rho(m_t, m_n). \quad [1]$$

This technique performs well in comparison to other self gating methods (13,14) and was selected as reference

[1]Department of Internal Medicine II, University Hospital of Ulm, Germany.
[2]Sirona Dental Systems, Imaging Systems, Bensheim, Germany.
[3]Department of Oral and Maxillofacial Surgery, University of Ulm, Germany.
*Correspondence to: Stefan Wundrak; Dipl. Inf. Department of Internal Medicine II, University Hospital of Ulm, Germany. E-mail: stefan.wundrak@uni-ulm.de

Received 10 June 2015; revised 1 September 2015; accepted 1 September 2015
DOI 10.1002/mrm.26000
Published online 00 Month 2015 in Wiley Online Library (wileyonlinelibrary.com).

© 2015 Wiley Periodicals, Inc.

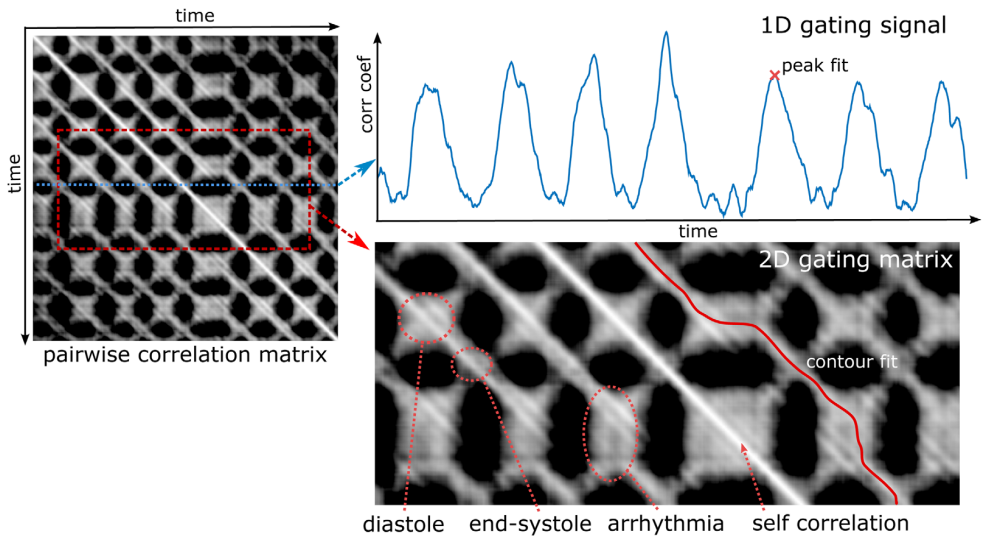

FIG. 1. Structure of the pair-wise correlation matrix D for an arrhythmic heart. Higher values indicate higher similarity of the template image (row) to the comparison image (column). The reference image is similar to images in the same position and same movement direction (lines parallel to the main diagonal) and in the same position and the opposite movement direction (lines orthogonal to the main diagonal). A row of the matrix equals the one-dimensional self-gating signal used in image-based self-gating (top). The peaks in the one-dimensional gating signal form curved lines in the two-dimensional gating matrix (bottom—red).

method for this work. The one-dimensional gating signal g is low-pass filtered using a temporal median filter with width σ. Peaks are detected to identify the zero-phase (trigger point) of each motion cycle. The k-space profiles are sorted into time frames based on the time interval to the neighboring peaks. The time frames are reconstructed frame-by-frame using gridding reconstruction. Cycles differing by more than $\Delta = 30\%$ in length from the mean cycle interval are rejected. The method is referenced as SG in the rest of this work.

Nonuniform Self-Gating

Overview

In case of nonreproducible motion cycles the SG method is not suitable, since k-space profiles of different motion phases will be sorted into the same bin. A nonuniform self-gating method (nuSG) with a weaker precondition is proposed, that presumes motion cycles that at least partially follow the same motion trajectory, possibly at a different pace. This motion model is expressed by curved line structures in a two-dimensional correlation matrix (see Fig. 1 and the following section). The suggested method comprises the following steps (see Fig. 2):

1. Acquire N golden angle radial k-space profiles
2. Reconstruct low spatial, high temporal resolution image series m
3. Restrict image series m to region of interest covering the moving anatomy of interest
4. Calculate pair-wise correlation matrix D for image series m
5. Fit active contours on line structures in D that indicate similar motion stages
6. Grow contours and detect gaps
7. Reconstruct cine images from k-space data selected by the active contours
8. Filter remaining streak artifacts

Contours in the Correlation Matrix

The $N \times N$ correlation matrix D is calculated using the pairwise Pearson correlation of all images in m, restricted to the region-of-interest region of interest.

$$D = (d_{r,c}); d_{r,c} = \rho(m_r, m_c). \quad [2]$$

Thus, each row r of D contains the one-dimensional gating signal from Eq. [1] using the template image m_r (Fig. 1). The two-dimensional gating matrix D for a cyclic moving object exhibits the rhombus structure shown in Figure 1. High correlation values indicate images in the same motion state as the reference image. The bright and straight main diagonal of the matrix result from the perfect similarity of each reference image to itself. If the object moved in identical cycles the matrix would exhibit perfectly straight lines parallel to the main diagonal. The nonuniform motion leads to curved lines that are only approximately parallel to the main diagonal. Lines approximately orthogonal to the main diagonal indicate images in the same motion state, but in the opposite motion direction of the reference image (e.g., *contraction* instead of *relaxation*).

Contour Fitting

If two motion cycles at least partially follow the same motion trajectory, possibly at a different pace, the correlation matrix exhibits a continuous and smooth line approximately parallel to the main diagonal. Therefore, smooth and continuous curves are fitted onto the line structures of D using active contour matching (15). The

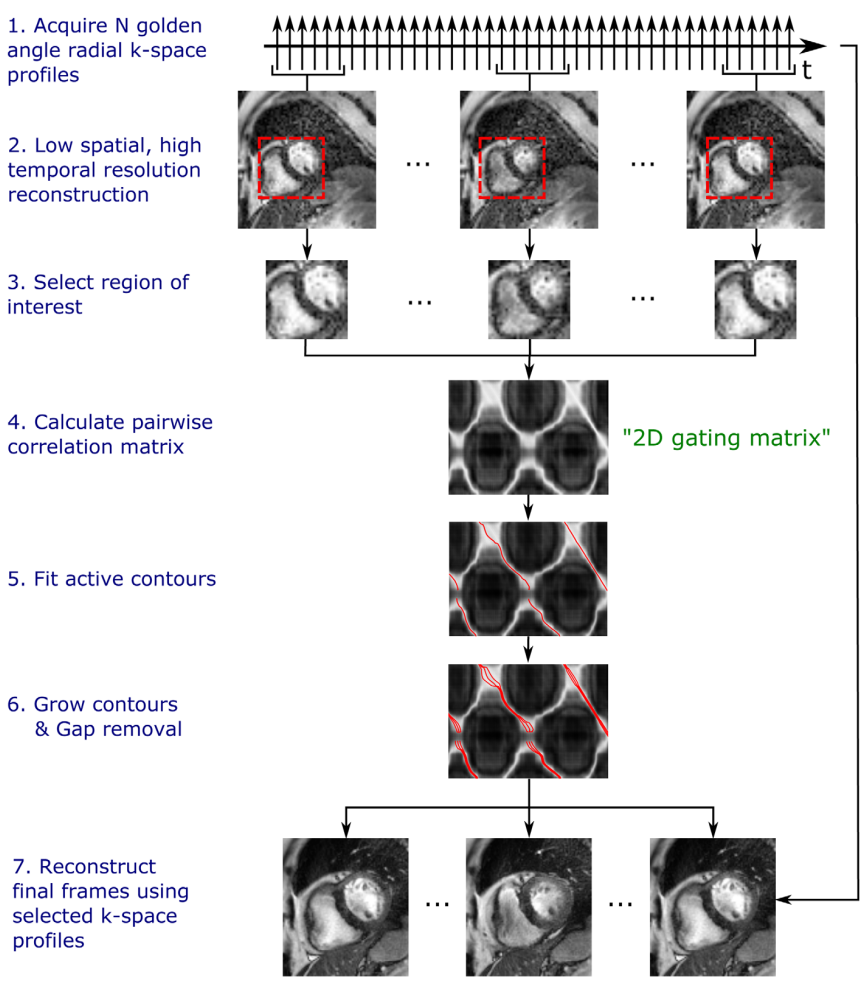

FIG. 2. Schematic overview of the proposed nuSG method.

one-dimensional parametric open active contour $v(r)$ specifies the column position for each row r of D.

$$E_{\text{cont}} = \sum_{r=1}^{N} E_{\text{int}}(v,r) + E_{\text{img}}(v,r) \qquad [3]$$

where the external energy term $E_{\text{img}}(v,r) = -d_{r,v(r)}$ forces the active contour toward the maxima of the correlation matrix D and the internal energy term E_{int} models the continuity and smoothness of the contour using the first- and second-order derivatives $E_{\text{int}}(v,r) = (\alpha|v'(r)|^2 + \beta|v''(r)|^2)/2$. The parameters α and β balance the tension and stiffness of the active contour. The active contour is relaxed using the Euler-Lagrange equation (see (16) for details).

Image Reconstruction

Each image x_r^* is reconstructed using all k-space profiles in a neighborhood w^* around the intersections $v_k(r)$ of all K contour lines with the row r of the correlation matrix D. In detail

$$x_r^* = \sum_{k=1}^{K} \sum_{n=v_k(r)-\frac{w^*}{2}}^{v_k(r)+\frac{w^*}{2}} G_n s_n \ , \qquad [4]$$

where G_n describes the linear gridding operator for the nth radial profile of a golden ratio trajectory (17), and s_n the corresponding sampling values. Due to the golden ratio acquisition scheme, the window w^* can be chosen independently from the window width w that was used to generate the undersampled images of the distance matrix D. The neighborhood w^* may be set to a fixed value to directly define the temporal resolution, or may be adapted such that the reconstructed images x_r^* are sampled using $w^* = \pi P m/(2C)$, where C is the actual number of cycles, m is the width of the acquisition matrix, and P the user defined sampling density. Remaining streak artifacts are filtered using a temporal total variation filter (18).

Grow Contours and Detect Gaps

If the motion path partially deviates from cycle to cycle, e.g., if in end-systole the myocardium did not fully contract, or the mandibula was not fully opened, or the TMJ exhibits "clicks," the line structures exhibit gaps (see Figs. 2 and 5). These gaps are detected by excluding values of the contour that are below a threshold γ relative to the mean of all correlation coefficients along the contour line.

If two frames have a similar ordering of radial profiles, the aliasing artifacts correlate and exhibit structures in the correlation matrix D parallel to the main diagonal. To avoid "locking" of the active contours during fitting to these superimposed structures in regions with broad correlation peaks (e.g., during a long resting phase), the neighborhood w^* is locally increased to cover δ percent of the correlation peak, where δ is a user defined parameter.

Feasibility Studies

The feasibility of the nuSG method was shown for the reconstruction of cardiac MRI data from patients with severe arrhythmia, and for assessment of the active motion of the TMJ. All studies were approved by the local ethics committee and written informed consent was obtained prior to the examination. All images were reconstructed using an in-house software package implemented with MATLAB (The MathWorks, MA).

For all scans a radial golden ratio profile ordering (17) was used, which proved to be beneficial for self-gating (13,19) by allowing a sliding window reconstruction with flexibility in the choice of the window width. Instead of the golden angle $\approx 111.246^\circ$ the smaller tiny golden angle $\approx 23.628^\circ$ was used (20) to avoid eddy current artifacts in combination with the balanced steady-state free precession sequence.

The parameters α and β for the active contours were optimized to fit the contour lines in all experiments as accurately as possible. The window width w was chosen to reach a trade-off between contrast and resolution in the gating matrix. The temporal median filter width was set to $\sigma = 2w$, which is a good trade-off between reduction of undersampling artifacts and temporal blurring. The grow threshold was set to $\delta = 95\%$ that prevented the locking to artifact correlation without influencing the temporal resolution during fast motion.

All datasets were additionally reconstructed using the real-time method *golden angle radial sparse parallel MRI* (GRASP) (21,22). The temporal regularization parameter λ was set to the smallest value that removed the radial undersampling artifacts in the region of interest.

Cardiac Experiment

Dynamic short axis time-resolved cardiac datasets were acquired from three patients (2 women, 1 man, aged 79–83 years) with known severe cardiac arrhythmia resulting in varying cardiac cycle length even during a short 6.3 s breathhold. Datasets were acquired on a Philips 1.5T Ingenia system (Philips Healthcare, Best, The Netherlands) with a 32-element cardiac coil. The acquisition parameters were: balanced steady-state free precession sequence, TR/TE = 2.6/1.3 ms, flip angle = 60°, resolution 1.7×1.7 mm^2, slice thickness 8 mm, acquisition matrix 212×212. The reconstruction parameters were 50 ms bin size for SG, $w = 23$, sampling window size $w^* = 20$, $\alpha = 0.001$, $\beta = 0.005$, and $\gamma = 66\%$ for nuSG. The reconstruction window of GRASP was also set to $w^* = 20$ profiles which equals a temporal resolution of 52 ms.

TMJ Experiment

Datasets from eight healthy volunteers (three women, five men, aged 21–51 years) were acquired. Further, seven patients with suspected TMJ derangement were scanned (six women, one man, aged 31–49 years). Sagittal images were acquired on a Philips 3T Achieva system (Philips Healthcare, Best, The Netherlands) using a 2×4 channel carotid coil (Chenguang Medical Technologies, Shanghai, China). The acquisition parameters were: in-phase balanced steady-state free precession, TE/TR = 2.3/4.6 ms, flip angle = 48°, pixel bandwidth of 949 Hz, spatial resolution of $0.75 \times 0.75 \times 5\,\text{mm}^3$, 256×256 pixel acquisition matrix, and a scan time of 60 s. The patients were instructed to continuously open and close the mouth within 8 s during the acquisition. The reconstruction parameters were 45 phases for SG, $w = 38$, $P = 75\%$, $\alpha = 0.001$, $\beta = 0.2$, and $\gamma = 66\%$ for nuSG. The window size of GRASP was set to w^* to achieve the same temporal resolution as nuSG.

Image Analysis

For each reconstructed image sequence, the image sharpness was calculated. For cardiac images, a profile was placed over the septal myocardial wall in the end-diastole frame as shown in Figure 3. For TMJ images the profile was placed over the condyle edge, in the center-frame between the open and the closed position. Edge sharpness was calculated as the mean intensity slope between the 20% and 80% signal level of the profile similar to (23). Significance of sharpness increase was assessed for TMJ using the one-sided Wilcoxon signed rank test. No significance tests were performed for cardiovascular magnetic resonance due to the small number of cases. A quantitative analysis of the left ventricular blood pool area was done using one short axis slice cine and standard software [Segment, Medviso, Lund, Sweden (24)].

RESULTS

Cardiac Experiment

Reconstructions were performed successfully in all cases. The number of rejected/detected cardiac cycles in SG was 2/5, 2/8, and 1/7, for the three patients, respectively.

A comparison between SG, nuSG, and GRASP reconstructions is provided in Figure 3 and as cardiac cines in the Supporting Information. The M-mode of SG clearly shows that the arrhythmic cycles are concealed, while for nuSG and GRASP all cycles are visible (asterisk). Visually, the images from SG have more residual streaking artifacts, especially in patient 1, and appear less sharp than the images from nuSG. The visual impression of increased wall sharpness in nuSG over SG is confirmed by quantitative evaluation (see Fig. 5), showing an increase of 80% on average for the three patients. In comparison to GRASP, nuSG also appears less noisy, as can be appreciated from the M-Mode plots, and sharpness is increased by 96% on average. The end-diastolic left ventricular blood pool area was on average 19.6 ± 2.9, 19.5 ± 1.4, $19.6 \pm 2.6\,\text{cm}^2$ for SG, nuSG,

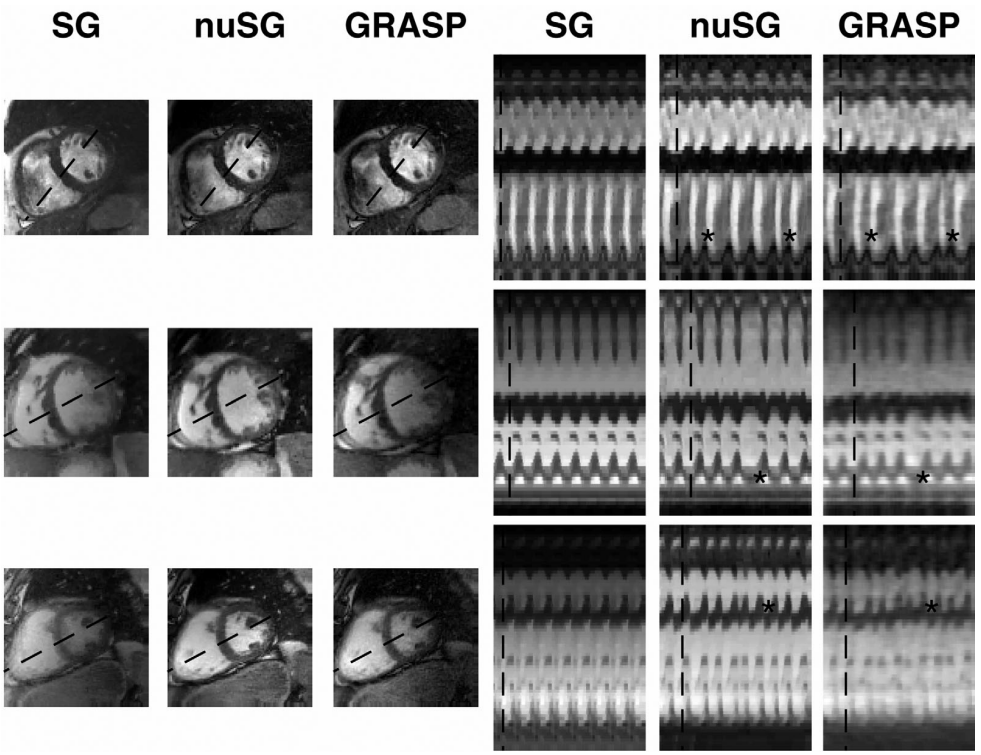

FIG. 3. Comparison of images (left columns) and M-modes (right columns) for the three reconstruction methods and for all arrhythmia patients (rows). The M-modes of the cardiac cine reconstructions (SG) (replicated for better visualization), indicates a single cyclic motion, while cardiac cycles of different length due to arrhythmia (asterisks) can be appreciated in the M-modes of nuSG and GRASP. Images from nuSG appear less noisy than from SG, as more k-space data was used for reconstruction, whereas in SG the cardiac cycles with arrhythmia had to be excluded from reconstruction. In GRASP only the k-space data of the current cardiac phase is used for reconstruction leading to increased noise, and due to temporal regularization to some temporal blurring. Cardiac cines for this figure are available as Supporting Information.

GRASP, respectively. The end-systolic area was on average 9.6 ± 3.1, 10.5 ± 1.4, $13.8 \pm 1.6\,\mathrm{cm}^2$, respectively.

TMJ Experiment

In comparison to SG, the proposed method resulted in improved image quality in all cases. Figure 4 shows four frames during the opening movement of the TMJ. Visual comparison of the two methods shows a clear improvement in image quality by nuSG for the moving condyle over SG and GRASP. The nuSG reconstruction provided sharp edges even during the phase of the fast condyle movement. In contrast, the SG reconstruction leads to strong blurring of the condyle. The M-mode plots show that the nuSG reconstruction is able to reproduce a higher temporal fidelity than SG and GRASP. Movies of the moving TMJ for volunteers and patients are available as Supporting Information.

Figure 5 summarizes the increase of image sharpness over the SG reconstructed images during the phase of condyle movement. The sharpness of the moving condyle edge was significantly increased by nuSG over SG for both groups ($P < 0.01$). The effective mean open/closing time was 4.2 ± 0.9 s for the volunteers and 3.9 ± 1.9 s for the patients. The temporal resolution based on the window width w^* was 180 ± 48 ms for the volunteers, and 176 ± 87 ms for the patients.

DISCUSSION

The poor results of the SG method show the limited feasibility of image-based self-gating methods in case of nonuniform motion. Even though only one self-gating variant was tested in this work, other variants like *center of mass kymogram* or *echo peak signal* (25) will likely lead to a similar result, as the underlying model of uniform motion cycles is not fulfilled.

In case of cardiac imaging, a rejection threshold is set to exclude arrhythmic cycles. Therefore, from the remaining uniform cycles, SG is usually still able to reconstruct cine images, however, with incomplete k-space data. The rejection threshold Δ, is a trade off between SNR and image sharpness. A low threshold excludes many cycles which leads to a low SNR or incomplete k-space. A high threshold keeps cycles that do not match which leads to image blurring and image artifacts. For example, patient 1 (Fig. 3) showed frequent extra-systoles and 40% of the cycles were rejected leading to low SNR and aliasing artifacts. Increasing the acquisition time was not an option due to breathhold limitations. In case of patient 3, the motion was even more irregular (fast and very irregular systoles) and the separation into valid and invalid cycles was not possible. In this case, SG is not able to reproduce any usable images (Fig. 3). In contrast, nuSG is able to use a larger

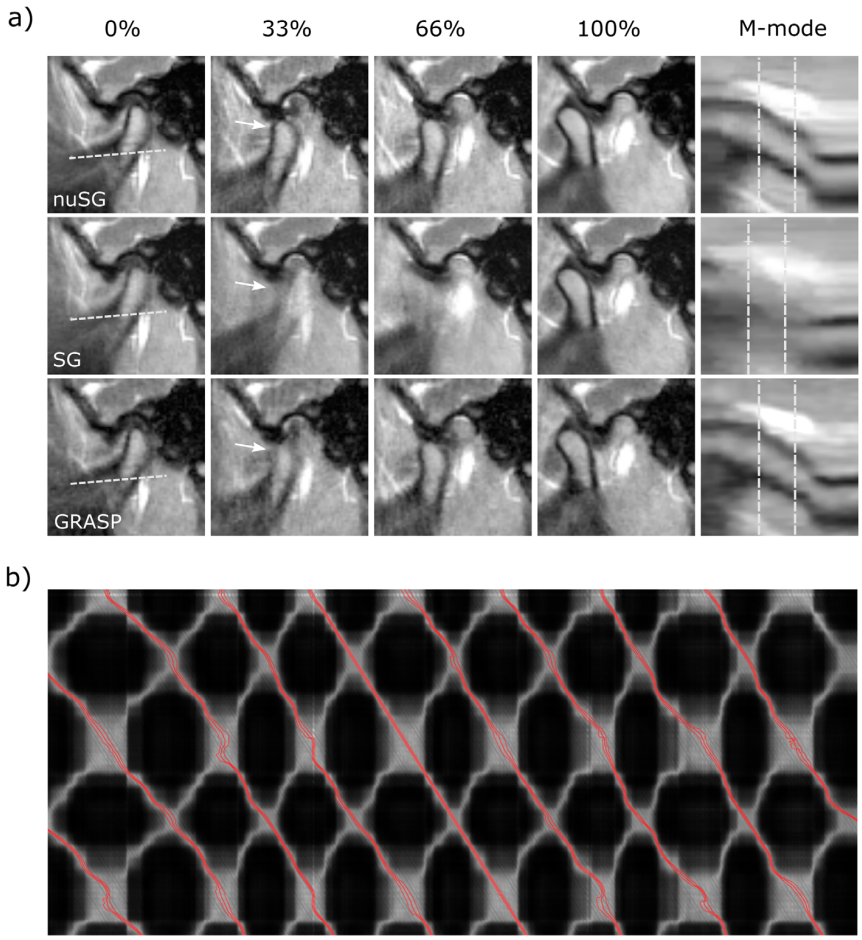

FIG. 4. **a**: Four equally spaced frames and M-mode plots of the opening TMJ reconstructed with nuSG, SG, and GRASP. The volunteer was opening the mouth within 3.4 s. The SG and iterative GRASP reconstruction show temporal blurring of the condyle (arrow). **b**: two-dimensional gating matrix of the same volunteer with active contours (red).

fraction of the acquired data, which leads to less aliasing and higher image sharpness.

As in the cine images reconstructed with GRASP, nuSG allows full appreciation of the arrhythmic heartbeats and shows all distinct cardiac cycles. In contrast, the SG method might misleadingly suggest a rhythmic heart. Even though real-time cine methods allow the acquisition without breath-hold, breath-hold acquisitions are day-to-day clinical routine and are justified for our method by the improved image quality of nuSG over GRASP.

The average end-diastolic volume was similar across the three methods, the end-systolic volume was overestimated by GRASP, which may be due to temporal regularization and leads to an underestimation of ejection fraction. Even though the number of cases were too small for any significance calculation, these results are in line with (9) and (1). In our experience, the proposed nuSG method is significantly less complex to implement, needs less computing power and is easier to parameterize than iterative real-time reconstruction methods.

In case of TMJ imaging, the proposed method allows the measurement of the TMJ opening/closing movement at a pace of about 8 s at $0.75 \times 0.75 \times 5\,\mathrm{mm}^3$ with little or no temporal blurring. Compared with previous work (26) where the same spatial resolution was used, this work shows about the same acquisition length and the same image quality, but a 9-fold increase in the nominal temporal resolution ($\approx$ 180 ms instead of 1655 ms). The effective temporal resolution may be lower, due to inaccuracy of the contour fitting. It still has to be evaluated how the method performs in case of sudden motion, like TMJ clicks (27), or in case of mastication under load (11).

Adaptive averaging methods (28,29) are related to image-based self-gating, in a sense that an image similarity function is used to identify subsets of images in an image sequence to be averaged. However, in adaptive

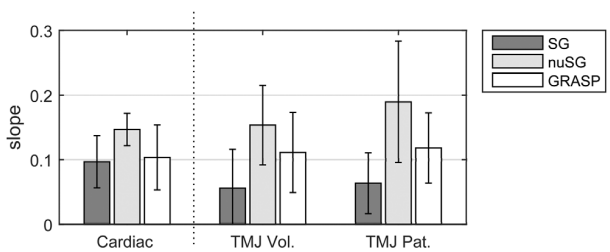

FIG. 5. Sharpness measured for three cardiac patients (on myocard wall), eight TMJ volunteers and seven TMJ patients (on condyle edge). TMJ sharpness for nuSG was significantly increased ($P < 0.01$) over SG; for cardiovascular magnetic resonance no significance was calculated due to the limited number of patients.

averaging no model of cyclic motion is used, and fully sampled images instead of partially sampled k-space views are combined.

In conclusion, a new self-gating method was proposed that allows cardiovascular magnetic resonance imaging of arrhythmic patients which is a common problem in clinical practice. Further, the proposed method enables SG imaging of the moving TMJ. More applications may be possible, e.g., SG imaging of the knee or wrist joint, or imaging of the soft palate.

ACKNOWLEDGMENTS

The authors thank Dr. Uta Denzel and Dr. Andreas Niedermayr for patient guidance. Stefan Wundrak and Jan Paul contributed equally to this work.

REFERENCES

1. Voit D, Zhang S, Unterberg-Buchwald C, Sohns JM, Lotz J, Frahm J. Real-time cardiovascular magnetic resonance at 1.5 T using balanced SSFP and 40 ms resolution. J Cardiovasc Magn Reson 2013;15:79.
2. Aandal G, Nadig V, Yeh V, Rajiah P, Jenkins T, Sattar A, Griswold M, Gulani V, Gilkeson RC, Seiberlich N. Evaluation of left ventricular ejection fraction using through-time radial GRAPPA. J Cardiovasc Magn Reson 2014;16:1–13.
3. Lanzer P, Barta C, Botvinick EH, Wiesendanger HUD, Higgins CB. ECG-synchronized cardiac MR imaging: method and evaluation. Radiology 1985;155:681–686.
4. Spraggins TA. Wireless retrospective gating: application to cine cardiac imaging. Magn Reson Imaging 1990;8:675–681.
5. Larson AC, White RD, Laub G, Mcveigh ER, Simonetti OP. Self-gated cardiac cine MRI. Magn Reson Med 2004;51:93–102.
6. Kellman P, Chefd'hotel C, Lorenz CH, Mancini C, Arai AE, McVeigh ER. High spatial and temporal resolution cardiac cine MRI from retrospective reconstruction of data acquired in real time using motion correction and resorting. Magn Reson Med 2009;62:1557–1564.
7. Krogh-Madsen T, Christin DJ. Nonlinear dynamics in cardiology. Ann Rev Biomed Eng 2012;14:179–203.
8. Webber CL. Nonlinear cardiac dynamics. In: Roka A, editor. Current issues and recent advances in pacemaker therapy. Rijeka: Intech; 2012. pp 233–246.
9. Wundrak S, Paul J, Ulrici J, Hell E, Rasche V. Does temporal regularization lead to systematic underestimation of ejection fraction? In: Proc Int Soc Magn Reson Med, Vol. 15. p 4380, Proceedings of the 22th Annual Meeting of ISMRM, Milano, 2014.
10. Burnett KR, Davis CL, Read J. Dynamic display of the temporomandibular joint meniscus by using 'fast-scan' mr imaging. Am J Roentgenol 1987;149:959–962.
11. Hopfgartner AJ, Tymofiyeva O, Ehses P, Rottner K, Boldt J, Richter EJ, Jakob PM. Dynamic MRI of the TMJ under physical load. Dentomaxillofac Radiol 2013;42.
12. Edwards AL. An introduction to linear regression and correlation. San Francisco, CA: W. H. Freeman, pp. 33–46, 1976.
13. Paul J, Divkovic E, Wundrak S, Bernhardt P, Rottbauer W, Neumann H, Rasche V. High-resolution respiratory self-gated golden angle cardiac MRI: comparison of self-gating methods in combination with k-t SPARSE SENSE. Magn Reson Med 2015;73:292–298.
14. Tibiletti M, Paul J, Bianchi A, Wundrak S, Rottbauer W, Stiller D, Rasche V, Multistage Three-Dimensional UTE Lung imaging by image-based self-gating. Magn Reson Med, doi:10.1002/mrm.25673.
15. Kass M, Witkin A, Terzopoulos D. Snakes: active contour models. Int J Comput Vis 1988;1:321–331.
16. Ivins J, Porril J. Everything you always wanted to know about Snakes (but were afraid to ask). Technical Report July 1993. Artificial Intelligence Vision Research Unit, University of Sheffield 2000.
17. Winkelmann S, Schaeffter T, Koehler T, Eggers H, Doessel O. An optimal radial profile order based on the golden ratio for time-resolved MRI. IEEE Trans Med Imaging 2007;26:68–76.
18. Rudin LI, Osher S, Fatemi E. Nonlinear total variation based noise removal algorithms. Phys D 1992;60:259–268.
19. Buerger C, Clough RE, King AP, Schaeffter T, Prieto C. Nonrigid motion modeling of the liver from 3-D undersampled self-gated golden-radial phase encoded MRI. IEEE Trans Med Imaging 2012;31:805–815.
20. Wundrak S, Paul J, Ulrici J, Hell E, Rasche VA. Small surrogate for the golden angle in time-resolved radial MRI based on generalized fibonacci sequences. IEEE Trans Med Imaging 2014;34.
21. Feng L, Grimm R, Tobias Block K, Chandarana H, Kim S, Xu J, Axel L, Sodickson DK, Otazo R. Golden-angle radial sparse parallel MRI: combination of compressed sensing, parallel imaging, and golden-angle radial sampling for fast and flexible dynamic volumetric MRI. Magn Reson Med 2013;72:707–717.
22. Wundrak S, Paul J, Ulrici J, Hell E, Geibel MA, Bernhardt P, Rottbauer W, Rasche V. Golden ratio sparse MRI using tiny golden angles. Magn Reson Med, doi:10.1002/mrm.25831.
23. Larson AC, Kellman P, Arai A, Hirsch GA, Mcveigh E, Li D, Simonetti OP. Preliminary investigation of respiratory self-gating for free- breathing segmented cine MRI. Magn Reson Med 2005;53:159–168.
24. Heiberg E, Sjögren J, Ugander M, Carlsson M, Engblom H, Arheden HK. Design and validation of Segment—freely available software for cardiovascular image analysis. BMC Med Imaging 2010;10:1–13.
25. Hardy CJ, Zhao L, Zong X, Saranathan M, Yucel EK. Coronary MR angiography: respiratory motion correction with BACSPIN. J Magn Reson Imaging 2003;17:170–176.
26. Zhang S, Gersdorff N, Frahm J. Real-time magnetic resonance imaging of temporomandibular joint dynamics. Open Med Imaging J 2011;5:1–7.
27. Scrivani SJ, Keith DA, Kaban LB. Temporomandibular disorders. N Engl J Med 2008;359:2693–2705.
28. Hardy CJ, Saranathan M, Zhu Y, Darrow RD. Coronary angiography by real-time MRI with adaptive averaging. Magn Reson Med 2000;44:940–946.
29. Scott AD, Boubertakh R, Birch MJ, Miquel ME. Adaptive averaging applied to dynamic imaging of the soft palate. Magn Reson Med 2013;70:865–874.

SUPPORTING INFORMATION

Additional Supporting Information may be found in the online version of this article.

Supporting Video 1: This supporting video shows the comparison of SG, nuSG, and GRASP for cardiac arrhythmia patient 1 from Figure 3.

Supporting Video 2: This supporting video shows the comparison of SG, nuSG, and GRASP for cardiac arrhythmia patient 2 from Figure 3.

Supporting Video 3: This supporting video shows the comparison of SG, nuSG, and GRASP for cardiac arrhythmia patient 3 from Figure 3.

Supporting Video S4: This supporting video shows the comparison of SG and nuSG for the TMJ reconstruction shown in Figure 4.

Supporting Videos S5 to S7: These supporting videos show the comparison of SG and nuSG for three TMJ patients. The first patient exhibits an anterior displacement of the disc without reposition at a flattened articular tubercle with an unphysiological and limited movement pattern. The second patient exhibits thinned structures between the condyle and the fossa articularis without recognizable physiological structure of the discus and a limited movement sequence. The third case exhibits an anatomical inconspicuous discus condyle relation. The movement terminates at the zenith of the articular tubercle.

7 Results and Discussion

In this thesis, respiratory and cardiac *Self-Gating (SG)* was investigated. Respiratory *SG* with *Compressed Sensing (CS)* reconstruction was utilized for *Tissue Phase Mapping (TPM)-Magnetic Resonance Imaging (MRI)*, and cardiac *SG* was used for comparison to and as the foundation of *Non-Uniform Self-Gating (nuSG)*.

First, different *SG* variants were investigated (see chapter 4). Compared to 0D-*SG* based on the k-space center or 1D-*SG* using single k-space profiles, image-based *SG* was shown to yield superior image sharpness. Thus, this technique using sliding window reconstruction was selected for combination with *TPM* (see chapter 5). While *Respiratory Navigator (RNAV)* measurements provide a respiratory signal independent of the imaging data, in *SG* the respiration information inherently depends on imaging parameters. However, image-based *SG* was shown to yield good breathing information and image quality over a variety of sequence parameters, such as *Fast Low Angle Shot (FLASH)* and *Balanced Steady-State Free Precession (bSSFP)*, short axis and long axis geometry, and black-blood and white-blood imaging. Additionally, *SG* was applied successfully for *TPM*, where the acquired temporal resolution of magnitude information is at least four times lower due to the interleaved measurements of the velocity encoding directions, resulting in higher undersampling for the generation of the *SG* image data.

SG-*TPM* allowed full application of blood saturation bands and thus resulted in superior contrast compared to *RNAV*-*TPM*, where the saturation had to be reduced in order to avoid interference with the navigator measurements (see chapter 5). Additionally, retrospective *Electrocardiogram (ECG)*-triggering in *SG*-*TPM* enabled reconstruction of the full cardiac cycle, also covering the "A" velocity peak in end-diastole, which cannot be measured with prospective trigger due to the acquisition break necessary to

accommodate heartbeat variations. Velocities calculated from the *SG* approach were highly similar to those obtained from the reference method.

CS reconstruction provided images without streaking artifacts for undersampling factors R of up to 8, which allowed reconstruction with high temporal resolution and/or reduction of acquisition time. Choice of the proper regularization strength λ was shown to be important not only for image quality, but also for the velocities reconstructed from *TPM* measurements, where too strong temporal regularization led to reduced velocity peaks. Selection of an appropriate balance between consistency of reconstructed and measured data on the one hand and model assumptions on the other hand, independent of imaging parameters and geometry, remains a major challenge for constrained reconstruction methods in general.

For cardiac *SG* (see chapter 6), higher temporal resolution of the *SG* images is required to resolve the motion during heartbeats (frequency $60 - 80\,\mathrm{min}^{-1}$) compared to respiratory motion (frequency $10 - 20\,\mathrm{min}^{-1}$), thus further increasing the undersampling in the *SG* image data. *SG* signals could also be extracted successfully for this application. Additionally, it was shown that the standard method of linear mapping the cardiac phases between the detected peaks (beginning of each cardiac cycle) led to deteriorated images in case of arrhythmia. This would also be the case with conventional *ECG* gating, since in both methods the model assumes a uniform motion with almost constant periodicity. *SG* was successfully extended to *nuSG* to be able to handle non-uniform motion, thus combining the advantages of good *Signal to Noise Ratio (SNR)* (as in gated cine imaging) and the temporal definition of realtime imaging (showing each, possibly irregular, motion cycle individually rather than an average cycle). Superior image sharpness was found in *nuSG* over *SG* and the *CS* sliding window reconstruction, which is due to absence of temporal averaging of different cardiac cycles and the absence of temporal regularization. Blood area measurements were comparable between *SG* and *nuSG*, but end-diastolic area was overestimated in the sliding window reconstruction due to the temporal smoothing effect of the *CS* approach.

Having evaluated the feasibility of *SG*-*TPM* with *CS*, further research could be directed to volumetric radial *TPM*. Isotropic 3D velocity information could be used for motion

analysis of the whole *Left Ventricle (LV)*. This might allow definition of new asynchrony parameters, which could further support patient selection and treatment decisions in a clinical setting, e.g. for *Cardiac Resynchronization Therapy (CRT)*. Additionally, the isotropic magnitude cine data could replace separate acquisitions performed for different views of the heart by retrospective reformatting, thus trading scan time for measurements only necessary in the current standard protocols. While the acquisition time for volumetric *TPM* is challenging, the *CS* reconstruction investigated for *TPM* in this thesis could allow to measure less data for reduction of scan time, thus making 3D *TPM* more practically usable.

Respiratory *SG* could also be utilized for reconstruction of data from different respiratory states. These images could then be aligned to a reference state via image registration, and motion-compensated reconstruction could be performed. Thus, overall gating efficiency would increase, allowing for further reduction of acquisition time, e.g. in the case of (volumetric) *TPM*.

Furthermore, cardiac *SG* could be combined with respiratory *SG*-*TPM*, thus eliminating the need for both *RNAV* and *ECG*. Alternatively, *nuSG* could be used as cardiac gating method for the assessment of myocardial motion velocities in patients with arrhythmia.

Bibliography

[1] Bernstein, M.A. ; King, K.F. ; Zhou, X.J.: *Handbook of MRI pulse sequences*. 1st edition. Amsterdam; Boston : Academic Press, 2004.

[2] Bijnens, B. ; Claus, P. ; Weidemann, F. ; Strotmann, J. ; Sutherland, G. R.: Investigating Cardiac Function Using Motion and Deformation Analysis in the Setting of Coronary Artery Disease. *Circulation* 116 (2007), 2453–2464.

[3] Brown, R.W. ; Cheng, Y.-C.N. ; Haacke, E.M. ; Thompson, M.R. ; Venkatesan, R.: *Magnetic resonance imaging: physical principles and sequence design*. 2nd edition. Hoboken, New Jersey : John Wiley & Sons, Inc, 2014.

[4] Cheung, Y.-F.: The role of 3D wall motion tracking in heart failure. *Nature reviews. Cardiology* 9 (2012), 644–657.

[5] Griswold, M.A. ; Jakob, P.M. ; Heidemann, R.M. ; Nittka, M. ; Jellus, V. ; Wang, J. ; Kiefer, B. ; Haase, A.: Generalized autocalibrating partially parallel acquisitions (GRAPPA). *Magnetic Resonance in Medicine* 47 (2002), 1202–1210.

[6] Lustig, M. ; Donoho, D.L. ; Santos, J.M. ; Pauly, J.M.: Compressed Sensing MRI. *IEEE Signal Processing Magazine* 25 (2008), 72–82.

[7] Lutz, A. ; Paul, J. ; Bornstedt, A. ; Nienhaus, G.U. ; Etyngier, P. ; Bernhardt, P. ; Rottbauer, W. ; Rasche, V.: Volumetric motion quantification by 3D tissue phase mapped CMR. *Journal of Cardiovascular Magnetic Resonance* 14 (2012), 1–13.

[8] Noll, D. C. ; Sutton, P. S.: Gridding Procedures for Non-Cartesian K-space Trajectories. Department of Biomedical Engineering, University of Michigan. http://web.eecs.umich.edu/~dnoll/gridding.pdf, Accessed: 2015-10-01.

[9] Paul, J.: *Berechnung und Analyse von Parametern zur Quantifizierung der Asynchronität des Herzschlages aus geschwindigkeitscodierten MRT-Aufnahmen*. Ulm, Ulm University, Diplomarbeit, 2011.

[10] Paul, J. ; Divkovic, E. ; Wundrak, S. ; Bernhardt, P. ; Rottbauer, W. ; Neumann, H. ; Rasche, V.: High-resolution respiratory self-gated golden angle cardiac MRI: Comparison of self-gating methods in combination with k-t SPARSE SENSE. *Magnetic Resonance in Medicine* 73 (2015), 292–298.

[11] Paul, J. ; Wundrak, S. ; Bernhardt, P. ; Rottbauer, W. ; Rasche, V.: Self-Gated Tissue Phase Mapping Using Golden Angle Radial Sparse SENSE. *Magnetic Resonance in Medicine* (2015). – DOI 10.1002/mrm.25669.

[12] Pelc, N.J. ; Bernstein, M.A. ; Shimakawa, A. ; Glover, G.H.: Encoding strategies for three-direction phase-contrast MR imaging of flow. *Journal of Magnetic Resonance Imaging* 1 (1991), 405–413.

[13] Pruessmann, K.P. ; Weiger, M. ; Scheidegger, M.B. ; Boesiger, P.: SENSE: sensitivity encoding for fast MRI. *Magnetic resonance in medicine* 42 (1999), 952–962.

[14] Rasche, V. ; Holz, D. ; Proska, R.: MR Fluoroscopy Using Projection Reconstruction Multi-Gradient-Echo (prMGE) MRI. 42 (1999), 324–334.

[15] Simpson, R. ; Keegan, J. ; Firmin, D.: Efficient and reproducible high resolution spiral myocardial phase velocity mapping of the entire cardiac cycle. *Journal of Cardiovascular Magnetic Resonance* 15 (2013), 34.

[16] Simpson, R. M. ; Keegan, J. ; Firmin, D.N.: MR assessment of regional myocardial mechanics. *Journal of Magnetic Resonance Imaging* 37 (2013), 576–599.

[17] Winkelmann, S. ; Schaeffter, T. ; Koehler, T. ; Eggers, H. ; Doessel, O.: An Optimal Radial Profile Order Based on the Golden Ratio for Time-Resolved MRI. *IEEE Transactions on Medical Imaging* 26 (2007), 68–76.

[18] Wundrak, S. ; Paul, J. ; Ulrici, J. ; Hell, E. ; Geibel, M.-A. ; Bernhardt, P. ; Rottbauer, W. ; Rasche, V.: A Self-Gating Method for Time-Resolved Imaging of Non-Uniform Motion. *Magnetic Resonance in Medicine* (2015). – DOI 10.1002/mrm.26000.

[19] Ypenburg, C. ; Van De Veire, N. ; Westenberg, J.J. ; Bleeker, G.B. ; Marsan, N.A. ; Henneman, M.M. ; Van Der Wall, E.E. ; Schalij, M.J. ; Abraham, T.P. ; Barold, S.S. ; J.J., Bax: Noninvasive Imaging in Cardiac Resynchronization Therapy–Part 2: Follow-up and Optimization of Settings. *Pacing and clinical electrophysiology* 31 (2008), 1628–1639.

[20] Ypenburg, C. ; Westenberg, J.J. ; Bleeker, G.B. ; Veire, N. Van d. ; Marsan, N.A. ; Henneman, M.M. ; Van Der Wall, E.E. ; Schalij, M.J. ; Abraham, T.P. ; Barold, S.S. ; Bax, J.J.: Noninvasive imaging in cardiac resynchronization therapy–part 1: selection of patients. *Pacing and clinical electrophysiology* 31 (2008), 1475–1499.

List of Figures

1 Cartesian and radial sequence diagrams and k-space 6
2 Comparison of undersampling artifacts 8
3 Principle of sliding window reconstruction. 10
4 Respiratory navigator 11
5 Sequence diagram for radial PC-MRI 14
6 Directional velocities on the myocardium 15
7 Electrocardiogram (ECG) 16

List of Tables

2 Comparison of Cartesian and radial MRI 10
3 Four-point balanced Hadamard encoding scheme 14

Acknowledgments

Content from this page was removed due to privacy reasons.

Curriculum Vitae

Content from this page was removed due to privacy reasons.

Journal Contributions

1. A. Lutz, J. Paul, A. Bornstedt, G. U. Nienhaus, P. Etyngier, P. Bernhardt, W. Rottbauer, and V. Rasche, Volumetric motion quantification by 3D tissue phase mapped CMR, Journal of Cardiovascular Magnetic Resonance, vol. 14, no. 1, pp. 1–13, 2012.

2. A. Lutz, J. Paul, A. Bornstedt, G. U. Nienhaus, P. Etyngier, P. Bernhardt, W. Rottbauer, and V. Rasche, Combination of tagging and tissue phase mapping to accelerate myocardial motion measurements in three directions, Magnetic Resonance Materials in Physics, Biology and Medicine, pp. 1–9, 2012.

3. J. Paul, E. Divkovic, S. Wundrak, P. Bernhardt, W. Rottbauer, H. Neumann, and V. Rasche, High-resolution respiratory self-gated golden angle cardiac MRI: Comparison of self-gating methods in combination with k-t SPARSE SENSE, Magnetic Resonance in Medicine, vol. 73, no. 1, pp. 292–298, Jan. 2015.

4. S. Wundrak, J. Paul, J. Ulrici, E. Hell, and V. Rasche, A Small Surrogate for the Golden Angle in Time-Resolved Radial MRI Based on Generalized Fibonacci Sequences, IEEE Transactions on Medical Imaging, vol. 34, no. 6, pp. 1262–1269, Jun. 2015.

5. J. Paul, S. Wundrak, P. Bernhardt, W. Rottbauer, H. Neumann, and V. Rasche, Self-Gated Tissue Phase Mapping using Golden Angle Radial Sparse SENSE, Magnetic Resonance in Medicine, doi: 10.1002/mrm.25669, 2015.

6. M. Tibiletti, J. Paul, A. Bianchi, S. Wundrak, W. Rottbauer, D. Stiller, and V. Rasche, Multi-stage three-dimensional UTE lung imaging by image-based self-gating, Magnetic Resonance in Medicine. doi:10.1002/mrm.25673, 2015.

7. S. Wundrak, J. Paul, J. Ulrici, E. Hell, M.A. Geibel, P. Bernhardt, W. Rottbauer, and V. Rasche, Golden Ratio Sparse MRI Using Tiny Golden Angles, Magnetic Resonance in Medicine, doi:10.1002/mrm.25831, 2015.

8. S. Wundrak*, J. Paul*, J. Ulrici, E. Hell, M.A. Geibel, P. Bernhardt, W. Rottbauer, and V. Rasche, A Self-Gating Method for Time-Resolved Imaging of Non-Uniform Motion. Magnetic Resonance in Medicine, doi: 10.1002/mrm.26000, 2015. ** = contributed equally*

Conference Contributions

1. A. Lutz, J. Paul, A. Bornstedt, G. Nienhaus, P. Etyngier, P. Bernhardt, W. Rottbauer, and V. Rasche, Volumetric motion quantification by 3D velocity encoded MRI, Journal of Cardiovascular Magnetic Resonance, vol. 14, no. Suppl 1, p. P247, 2012.

2. A. Lutz, S. Kozerke, J. Paul, M. Schmucker, A. Bornstedt, G. U. Nienhaus, W. Rottbauer, and V. Rasche, Applicability of k-t BLAST, k-t SENSE, k-t PCA and k-t PCA/SENSE for tissue phase mapping in a heart phantom at 3T, presented at the ISMRM, Melbourne, 2012, p. 4202.

3. A. Lutz, J. Paul, P. Etyngier, A. Bornstedt, P. Bernhardt, G. Nienhaus, W. Rottbauer, and V. Rasche, Quantitative assessment of myocardial motion from velocity encoded MRI, Journal of Cardiovascular Magnetic Resonance, vol. 14, no. Suppl 1, p. W39, 2012.

4. A. Lutz, J. Paul, P. Etyngier, A. Bornstedt, G. Nienhaus, P. Bernhardt, W. Rottbauer, and V. Rasche, Quantitative assessment of myocardial motion from displacement measurements derived from velocity encoded MRI, Journal of Cardiovascular Magnetic Resonance, vol. 14, no. Suppl 1, p. W20, 2012.

5. J. Paul, A. Lutz, P. Bernhardt, P. Etyngier, W. Rottbauer, and V. Rasche, Left Ventricular Asynchrony Quantification by Means of Myocardial Displacement Derived from Velocity Encoded MRI, presented at the ISMRM, Melbourne, 2012, p. 3800.

6. S. Wundrak, J. Paul, J. Ulrici, E. Hell, and V. Rasche, Retrospective Self-Gated MRI of the TMJ Dynamics During Mastication, presented at the ISMRM, Salt Lake City, 2013, p. 3165.

7. R. Beck, J. Paul, A. Müller-Lutz, D. Buckert, P. Bernhardt, W. Rottbauer, and V. Rasche, Quantitative comparison of left ventricular motion parameters for the assessment of asynchrony and motion abnormalities, Journal of Cardiovascular Magnetic Resonance, vol. 16, no. Suppl 1, p. P94, 2014.

8. J. Paul, E. Divkovic, S. Wundrak, P. Bernhardt, W. Rottbauer, H. Neumann, and V. Rasche, High Resolution Respiratory Self-Gated Golden Angle Cardiac MRI: Comparison of Self-Gating Methods in Combination with k-t SPARSE SENSE, presented at the ISMRM, Milano, 2014, p. 4361.

9. J. Paul, S. Wundrak, P. Bernhardt, W. Rottbauer, and V. Rasche, Accelerated radially encoded tissue phase mapping, Journal of Cardiovascular Magnetic Resonance, vol. 16, no. Suppl 1, p. W21, 2014.

10. M. Tibiletti, J. Paul, D. Stiller, and V. Rasche, Relevance of respiratory gating for proton Lung MRI, presented at the ISMRM, Milano, 2014, p. 3548.

11. S. Wundrak, J. Paul, J. Ulrici, E. Hell, S. Kozerke, and V. Rasche, Sparse Dynamic MRI with an Adaptive Temporal Sparsity Prior for Cardiovascular Imaging, presented at the ISMRM, Milano, 2014, p. 4384.

12. S. Wundrak, J. Paul, J. Ulrici, E. Hell, and V. Rasche, Does Temporal Regularization Lead to Systematic Underestimation of Ejection Fraction?, presented at the ISMRM, Milano, 2014, p. 4380.

13. S. Wundrak, J. Paul, J. Ulrici, E. Hell, and V. Rasche, Sparse Dynamic MRI of the Temporomandibular Joint, presented at the ISMRM, Milano, 2014, p. 1267.

14 J. Paul, R. Beck, D. Buckert, P. Bernhardt, W. Rottbauer, H. Neumann, and V. Rasche, Left ventricular motion quantification parameters from tissue phase mapped MRI: influence of gender, Journal of Cardiovascular Magnetic Resonance, vol. 17, no. Suppl 1, p. Q20, 2015.

15. J. Paul, S. Wundrak, P. Bernhardt, W. Rottbauer, H. Neumann, and V. Rasche, Self-Gated Tissue Phase Mapping using Golden Angle Radial Sparse SENSE, presented at the ISMRM, Toronto, 2015, p. 1052.

16. J. Paul, S. Wundrak, H. Neumann, and V. Rasche, Sub-Millimeter Motion-Corrected Tissue Phase Mapping for Transmural Analysis of LV Motion, presented at the ISMRM, Toronto, 2015, p. 1047.

17. J. Paul, S. Wundrak, H. Neumann, and V. Rasche, Coil Array Compression for Tissue Phase Mapping, presented at the ISMRM, Toronto, 2015, p. 1040.

18. J. Paul, P. Bernhardt, H. Neumann, and V. Rasche, Radial Tissue Phase Mapping is more Robust against In-flow Effects than Cartesian Tissue Phase Mapping, presented at the ISMRM, Toronto, 2015, p. 558.

19. S. Wundrak, J. Paul, J. Ulrici, E. Hell, M.-A. Geibel, and V. Rasche, MRI of the moving TMJ using Contour Fitting in the Correlation Matrix (CoFi-CoMa), presented at the ISMRM, Toronto, 2015, p. 2085.

20. S. Wundrak, J. Paul, J. Ulrici, E. Hell, and V. Rasche, Tiny Golden Angles: A Small Surrogate for the Radial Golden Angle Profile Order, presented at the ISMRM, Toronto, 2015, p. 2085. *(ISMRM Magna Cum Laude Award)*

21. M. Tibiletti, J. Paul, A. Bianchi, S. Wundrak, W. Rottbauer, D. Stiller, and V. Rasche, Multi-stage three-dimensional UTE lung imaging by image-based self-gating, presented at the ISMRM, Toronto, 2015, p. 2386.

22. J. Paul, V. Schmitt, S. Wundrak, M. Radermacher, V. Hombach, P. Bernhardt, W. Rottbauer, and V. Rasche, Realtime Cardiac Function using Compressed Sensing: Initial Clinical Evaluation. Accepted for presentation at the SCMR, Los Angeles, 2016.

23. S. Wundrak, J. Paul, M. Radermacher, V. Hombach, W. Rottbauer, P. Bernhardt, and V. Rasche, High-quality reconstruction of arrhythmic cardiac cycles. Accepted for presentation at the SCMR, Los Angeles, 2016.